Engineering Structures 270 (2022) 114067

Contents lists available at ScienceDirect

Engineering Structures

journal homepage: www.elsevier.com/locate/engstruct

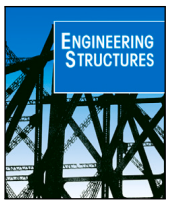

Aero-structural optimization-based tailoring of bridge deck geometry

M. Cid Montoya [a,*], S. Hernández [b], A. Kareem [c]

[a] Department of Engineering, Texas A&M University-Corpus Christi, Corpus Christi, TX, 78412, USA
[b] Structural Mechanics Group, School of Civil Engineering, University of La Coruña, 15071, La Coruña, Spain
[c] NatHaz Modeling Laboratory, Department of Civil and Environmental Engineering and Earth Sciences, University of Notre Dame, Notre Dame, IN, 46556, USA

ARTICLE INFO

Keywords:
Aero-structural optimization
Aeroelasticity
Buffeting
Wind-resistant design
Surrogate models
Deck shape
Bridge engineering

ABSTRACT

The deck cross-section is usually identified in engineering practice as the most important design variable in the wind-resistant design of long-span bridges. This is certainly true in most cases since it controls the aerodynamic and mechanical contribution of the deck to the global bridge performance. However, the effectiveness of deck shape modifications to handle the aeroelastic constraints is highly influenced by the aeroelastic performance requirements. This paper seeks to delve into the aero-structural design optimization of long-span bridges by analyzing possible design scenarios depending on the ability of the deck shape to meet the imposed aeroelastic requirements. A long-span cable-stayed bridge is optimized focusing on the buffeting response and considering different sets of limit values for the design constraints. According to the effectiveness of the deck shape design variables and other size design variables to manage the aeroelastic design constraints, three types of aero-structural optimization problems are identified: type I, aeroelastic constraints are not active and structural constraints drive the design; type II, aeroelastic constraints are active and effectively controlled by deck shape modifications; and type III, aeroelastic constraints are active and demand both shape and size modifications. The engineering significance for practical design is discussed.

1. Introduction

Structural optimization has been possible since the 1960s, when optimization theory, structural analysis, and computer hardware were integrated, giving rise to what was defined in those days as structural synthesis (Schmit [1,2]). Later, in the 1970s, gradient-based optimization algorithms were applied for the first time to the aerodynamic shape optimization of aircraft wings (Hicks et al. [3] and Hicks and Henne [4]). This technique has been further developed in the aerospace research field and industry to the present day, and a large amount of research has been published dealing with both aerodynamic shape optimization (Reuther et al. [5] and Lyu et al. [6]) and aero-structural shape optimization (Martins et al. [7] and Jasa et al. [8]) of aircraft wings.

Despite the positive environmental and economic impact of structural optimization (Lagaros [9]), the application of computational design techniques in wind engineering is still in the developmental phase, but it has been gaining momentum (Kareem [10]). In recent years, research about aerodynamic shape optimization was developed for tall buildings (Bernardini et al. [11], Elshaer et al. [12] and Ding and Kareem [13]), high-speed trains (Li et al. [14] and Muñoz Paniagua and García [15]), and barriers for windblown sand mitigation (Horvat et al. [16]).

In the bridge engineering field, the application of structural optimization approaches is scarce and primarily confined to research activities. It is difficult to find existing civil structures whose design has been conducted using optimization algorithms. One example is a 300 m footbridge built on the campus of the University of Aveiro, Portugal, where the location of the nodes of its truss beam was defined by an optimization algorithm (Azevedo et al. [17]). In the case of cable-supported bridges, the first applications at the research level of structural synthesis were carried out in the 1990s by Simões and Negrão [18], optimizing different elements of a cable-stayed bridge considering design constraints related to gravitational loads. Later, Baldomir et al. [19] presented a formulation for the estimation of the optimum prestressing forces of the stays of a cable-stayed bridge without inner loops in the optimization process, which allows the efficient optimization of the cable supporting system. The determination of optimum cable forces is an important design task that affects the overall design of the bridge, and several authors have contributed to this topic thus far, e.g. Hassan et al. [20]. Further developments in the optimization of cable supporting systems and bridge deck designs considering structural constraints have addressed the specific challenges of each bridge typology. Interesting contributions can be found in Lonetti and Pascuzzo [21], which deals with the optimum design of

* Corresponding author.
E-mail addresses: miguel.cidmontoya@tamucc.edu (M. Cid Montoya), hernandez@udc.es (S. Hernández), kareem@nd.edu (A. Kareem).

https://doi.org/10.1016/j.engstruct.2022.114067
Received 30 June 2021; Received in revised form 19 January 2022; Accepted 22 February 2022
Available online 30 March 2022

hybrid cable-stayed suspension bridges, Fabbrocino et al. [22], which carries out a pre-tensioning optimization of lattice structures forming composite cable-stayed bridges, and Arellano et al. [23], where the design optimization of criss-cross cables was addressed, among many others.

Furthermore, multidisciplinary optimization approaches were developed in order to include design constraints different from the classical behavior constraints related to structural responses under gravitational loads. For instance, the first application of optimum design taking into account hazardous phenomena was reported by Simões and Negrão [24], considering earthquake-related design constraints. Later applications adopting dampers to mitigate earthquake effects were authored by Ferreira and Simões [25]. In recent contributions by Ferreira and Simões [26], the dynamic lock-in phenomenon caused by pedestrian loading in footbridges has been considered in the optimization problem. A comprehensive review of cable-stayed bridge optimization can be found in Martins et al. [27].

Focusing on the aeroelastic phenomena (Larsen and Larose [28]), the first contribution to the gradient-based aeroelastic design of bridges was developed by Jurado and Hernández [29] in the 2000s. Sensitivity analyses provided the qualitative and quantitative relationships between flutter response and several mechanical properties, such as the positive effect of augmenting the torsional inertia to increase the flutter speed. This was carried out taking advantage of the advances in the multi-mode flutter analyses of bridges developed in the 1990s by Agar [30] and Katsuchi et al. [31]. Later, some other investigations deepened in this approach, conducting further sensitivity analyses or parameter variation studies to ascertain the influence of relevant parameters of the bridge on its flutter velocity (see, for instance, Zhang [32] and Argentini et al. [33]).

Nevertheless, the first contribution reporting the optimization of a long-span bridge including an aeroelastic design constraint was the paper by Nieto et al. [34], where kinematic and flutter constraints were considered to optimize the size of the deck plates thicknesses of the Messina Bridge project. Later, in the recent investigations by Kusano et al. [35], this approach has been extended to have into account the inherent uncertainties in the identification of the flutter derivatives (see Sarkar et al. [36]), leading to the formulation of a probabilistic aeroelastic optimization problem.

However, in the aforementioned research studies, the girder geometry, which is one of the most important aspects in aeroelastic design, was not adopted as a shape design variable, constraining the ability of the optimization algorithm to effectively improve the design. This issue was addressed in the authors' previous contributions (Cid Montoya et al. [37] and Cid Montoya et al. [38]), focusing on flutter-resistant design. The core idea was to develop an alternative approach to the classical design process of long-span bridges (see Chen and Duan [39]) aiming at achieving more efficient designs taking into account wind-induced effects. In Cid Montoya et al. [37], a fully numerical procedure was developed by combining CFD simulations with surrogate models, and estimating the aeroelastic loads acting on streamlined bridge decks by taking advantage of the quasi-steady (QS) formulation (Scanlan [40] and Chen and Kareem [41]). This methodology enabled the numerical assessment of the bridge flutter velocity as a function of the deck shape. Validated results showed the impact of the fairing angle, which was controlled by the width of the single-box deck cross-section, on the deck aerodynamics and the bridge flutter speed. Later, in Cid Montoya et al. [38], the formulation for the aero-structural shape optimization problem considering flutter was presented and successfully applied. The combined design demands of structural and flutter requirements highlighted the importance of the deck depth given its positive contribution to the bridge stiffness without worsening the aeroelastic characteristics in the considered design domain.

Long-span bridges need to be safe enough to withstand any relevant wind induced effect. Accordingly, this paper addresses the performance of bridges under buffeting (Hui et al. [42], Zasso et al. [43] and Lystad et al. [44]). This aeroelastic phenomenon caused by the inherent turbulence in the flow field affects the bridge's performance throughout its service life. Buffeting-induced accelerations on the deck can cause instability of vehicles or discomfort to pedestrians (ISO 2631 [45]), which is a serviceability limit state, and stress and fatigue damages (Zhu et al. [46] and Repetto and Torrielli [47]), which are ultimate limit states. These responses are usually managed by designers by setting thresholds to the lateral, vertical, and torsional accelerations at several control points along the bridge deck for several wind velocities to address different scenarios (Stretto di Messina [48]). This leads to the consideration of a large number of responses that may require contradictory modifications in the buffeting-resistant design, in contrast to the flutter-resistant design where the only response to handle is the critical wind speed. The long-term goal of this research effort is to further develop an aero-structural optimization framework including not only these two phenomena but also vortex-induced vibrations (VIV) (Larsen and Poulin [49] and Diana et al. [50]), which also needs to be analyzed against being overstressed and fatigue strength on the deck members, and aerostatic stability (Boonyapinyo et al. [51]), which is an aerodynamic instability that can be a more restrictive ultimate limit state than flutter (Nagai et al. [52]).

It must be remarked the importance of adopting an adequate formulation for the aero-structural optimization problem in bridge design. In several engineering fields, the aerodynamic shape optimization problem is commonly formulated as a minimization of the aerodynamic loads. Applications can be found in multiple disciplines, such as in road vehicles (Muyl et al. [53]), where different parts of the car shape are optimized seeking the reduction of the drag, high-speed trains (Muñoz Paniagua and García [15]), where the shape of the head is optimized to minimize the drag and lift when running in the open air and the pressure pulse of two trains passing by, and tall buildings (Bernardini et al. [11], Mooneghi and Kargarmoakhar [54] and Elshaer et al. [12]), where the building cross-section shape is optimized to minimize the drag. These contributions demonstrated the effectiveness of shape optimization techniques to minimize the aerodynamic loads. On the contrary, in the field of wind energy generation, such as wind turbines design, the goal is to maximize the aerodynamic performance, or more specifically, the energy production (Chehouri et al. [55]). In aerospace engineering, the classic wing aerodynamic shape optimization problem seeks the minimization of the drag subject to some constraints which also involve the lift and moment coefficients (see, for instance, Hicks and Henne [4], Lyu et al. [6] and Skinner and Zare-Behtash [56]). In aircraft aero-structural shape optimization frameworks, the objective function also includes the weight of the structure (Martins et al. [7]).

On the other hand, according to Martins et al. [27], pure structural optimization frameworks for cable-stayed bridges have mainly focused on two key topics: (1) ''cable-forces optimization'', and (2) ''optimum design'' aiming at minimizing the cost of the bridge. A comprehensive aero-structural shape optimization framework for the design of cable-stayed bridges should address these two goals but also consider the aeroelastic phenomena affecting the bridge performance. Hence, the aeroelastic responses should be formulated in the bridge engineering field as they are considered in real projects. As it can be seen, for instance, in the specifications for the Messina Strait Bridge (Stretto di Messina [48]), the aeroelastic responses are limited by imposing specific thresholds. Therefore, they must be considered in the optimization problem as design constraints adopting as limit values the thresholds set in each particular project. Depending on the limit values adopted, the wind conditions at the bridge location, and the bridge design, the aeroelastic constraints can play either an active or passive role in the design process, which would result in different optimum designs. Moreover, the sensitivity of the aeroelastic responses with the deck shape will determine the capability of the deck shape design variables to act as effective passive countermeasures to achieve safe designs. These two aspects will impact the optimization outcome and their influence on the optimum deck shape must be further investigated.

This study addresses the aero-structural optimization problem of long-span bridges considering shape and size design variables in the deck cross-section, and size variables in the cable-supporting system. This set of design variables permits the control of both deck aerodynamics and its stiffness and mass contribution to the global bridge properties, as well as the stiffness contribution of the cable-supporting system. The importance of these factors for controlling the aeroelastic performance was summarized by Larsen and Larose [28] as "*Aeroelasticity is roughly 20% aero- and 80% elasticity*" to highlight the importance of the structural dynamics contribution to the aeroelastic response. On the other hand, the structural and aeroelastic performances, particularly buffeting accelerations, are considered design constraints. The impact of the limits adopted for the aeroelastic constraints on the optimum deck shape, as well as the capability of the deck shape design variables to mitigate these aeroelastic responses, are investigated. While this study is carried out in the frame of optimization problems, the concepts developed from this research can be generalized for wind-resistant design problems involving shape design variables.

The methodology for the buffeting-resistant aero-structural shape design of bridge decks was presented and formulated in a previous contribution (Cid Montoya et al. [57]), including the description of the surrogate model, CFD simulations, and buffeting analysis. The wind load model was formulated and its applicability for the design of long-span bridges was discussed based on measured flutter derivatives. Furthermore, parametric studies were conducted to investigate the relationship between the buffeting response of a single-box deck cable-stayed bridge and deck shape-dependent properties, such as deck stiffness, mass, and aerodynamics. It was found that the width of the deck, which controls the fairing angle and consequently the influential χ^*_{Dw}, χ^*_{Lw} and χ^*_{Mw} admittance functions, is very effective to mitigate the RMS of torsional and vertical accelerations of the bridge. Increasing the deck width leads to a decrease in the vertical response in exchange for increasing the torsional acceleration, while decreasing the deck width diminishes the torsional response. Hence, buffeting-resistant design entails taking trade-off decisions while considering the specific design parameters of each project. This makes optimization algorithms a powerful tool for addressing these challenges in the preliminary design stages of long-span bridges. In the present article, the methodology for the aero-structural shape optimization is conceptually introduced in Section 2, and the formulation is later developed in Section 3, where the specific characteristics of buffeting-resistant design optimization are addressed. The long-span cable-stayed bridge with a streamlined single-box deck cross-section used as an application example is described in Section 4. In Section 5, the buffeting responses of the optimum structural designs at the four wind velocities under study are presented along with shape parametric studies. Result are compared to the thresholds imposed for each wind velocity. This advances the results and design conclusions learned from parametric studies in previous investigations, since the relationship between the design variables and the buffeting responses are obtained after the design has been polished. This information is instrumental for the adequate interpretation of the optimum designs obtained in the frame of the complete aero-structural optimization of the bridge, which are reported in Section 6. Finally, the influence of the chosen set of aeroelastic design constraints on the optimum aero-structural design is discussed, leading to the definition of three types of aero-structural optimization problems depending on the behavior of the deck shape design variables. The validity of this classification is analyzed using the results of this study as well as the flutter-resistant optimization previously carried out in Cid Montoya et al. [38]

2. Aero-structural optimization framework considering shape and size design variables

This section describes the numerical framework that permits the formulation of an optimization problem aiming at obtaining the optimum bridge deck shape and plates' size design, along with the optimal cable supporting system. The goal is to achieve sustainable, economical, and safe designs by minimizing the weight of the structure while accomplishing all the design constraints, including those related to gravitational loads and those related to buffeting-induced responses. In this context, the numerical evaluation of all the structural and aeroelastic responses of the bridge is a cardinal requirement. For this reason, this investigation takes advantage of the numerical procedure developed in Cid Montoya et al. [57] for the evaluation of the buffeting response of long-span bridges within a numerical design framework.

The first step to carry out the aero-structural optimization (Fig. 1) is the proper definition of the problem including the objective function, design variables (initial design and ranges of variation), design constraints, and design parameters (e.g. wind modeling). This conditions the following two steps, which are the construction of a parametrized finite element model (FEM), and a validated aerodynamic surrogate model (ASM). In the first case, the FEM will be responsible for providing for any combination of input design variables the required output, which includes displacements and stress responses for multiple control points and load cases, as well as modal data for the multi-mode aeroelastic analyses. In the second case, the ASM will have as input the deck shape design variables that control the deck aerodynamics, and the output will be the aerodynamic parameters required to obtain the aeroelastic responses. The construction of the ASM is conditioned by the definition of the problem, particularly by the lower and upper bound of the shape design variables, which define the shape design domain. Then, a sampling plan is carried out to set the designs that will be evaluated by means of CFD simulations to train the surrogate model. It must be remarked the importance of experimental validation and time and space verification of the CFD simulations to guarantee the accuracy of the surrogate model.

Once the FEM and ASM are available, the optimization framework can be developed by implementing a numerical scheme able to produce all the structural (e.g. kinematic and stress responses related to self-weight and service loads) and aeroelastic responses (e.g. buffeting accelerations) required in the formulation of the design constraints (output) for each set of design variables proposed by the optimization algorithm (input). This is defined in Fig. 1 as Bridge Multidisciplinary Analysis (BMA). First, a set of static analyses using the finite element model (FEM) of the full bridge are conducted for each gravitational load case. These can include self-weight and traffic service loads, and the responses are usually of kinematic and stress nature. Second, the procedure for obtaining the buffeting responses must be implemented, as shown in Fig. 1. This involves solving the eigenvalues problem using the FEM of the full bridge to obtain the natural frequencies and mode shapes. Then, taking advantage of the ASM and the quasi-steady formulation (Scanlan [40], Chen and Kareem [41] and Kavrakov and Morgenthal [58]), the aeroelastic self-excited and buffeting forces acting on streamlined bridge decks can be obtained from the approximated flutter derivatives and admittance functions. Then, the buffeting responses can be assessed by solving the multi-mode buffeting analysis using the information previously obtained and the specific wind model defined for the project under study. In this manner, all the responses required are available, providing the algorithm with all the required information to iteratively improve the design until reaching convergence. It must be highlighted that the independence of most of the procedures included in the BMA allows the application of parallel computing to reduce the computation burden. While this study is focused on the buffeting-resistant design of long-span bridges, the methodology is very versatile and can be further extended to include additional design constraints. Future investigations will address the aero-structural optimization problem considering additional aeroelastic responses, such as VIV and nonlinear aerostatic stability, by suitably extending the BMA to obtain the required responses.

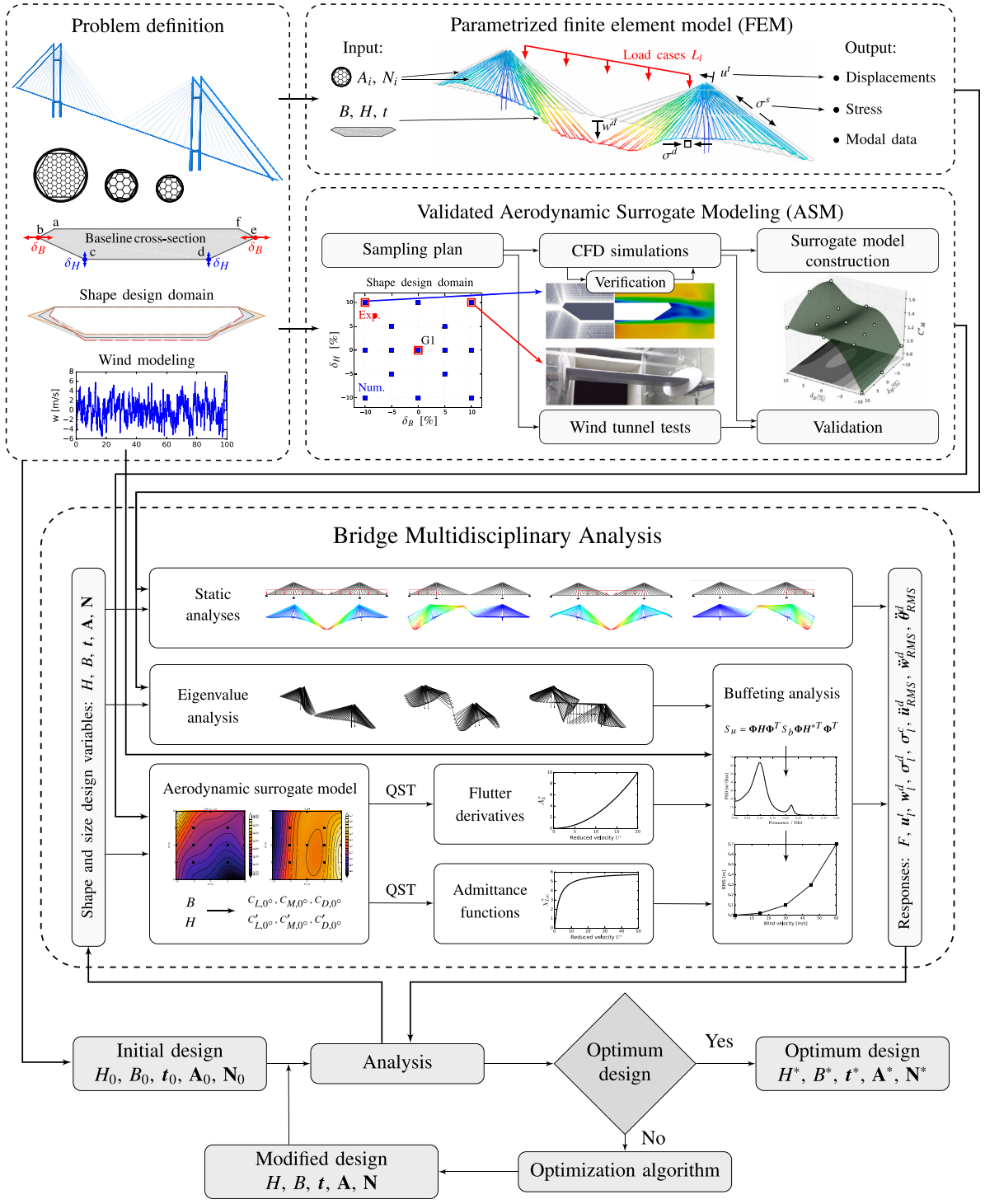

Fig. 1. Flowchart of the methodology for carrying out the aero-structural optimization. (For interpretation of the references to color in this figure legend, the reader is referred to the web version of this article.)

3. Formulation of the aero-structural optimization problem

The aero-structural optimization of long-span bridges can be formulated as a constrained optimization problem where the objective function $F(\mathbf{x})$ is the property of the bridge to be minimized, commonly a sustainability or economical cost related quantity such as the weight or volume of the structure. The objective function depends on a set of design variables $\mathbf{x}$, which are the properties of the bridge that the optimization algorithm can modify to achieve its goal. This problem is subject to lateral constraints ($\mathbf{x}_{min} \leq \mathbf{x} \leq \mathbf{x}_{max}$), which establish the range of variation enabled for each design variable; and also to a number of design constraints ($g_i(\mathbf{x}) < 0$, $i = 1...m$), which are the structural and aeroelastic performance requirements to be fulfilled by candidate designs. Since the responses of the bridge belong to different disciplines, this problem can be labeled as a multidisciplinary optimization problem (Martins and Lambe [59]). The formulation adopted to conduct the aero-structural optimization is posed to be solved using gradient-based optimization algorithms.

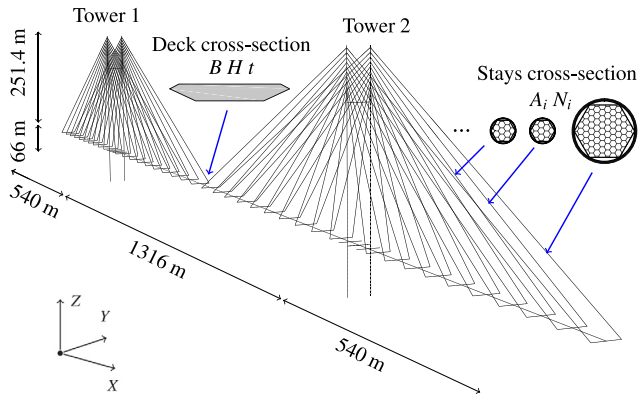

Fig. 2. Layout of the bridge FEM.

The optimization algorithm used is Sequential Quadratic Programming (SQP). The objective function is formulated as:

$$\min F(\mathbf{x}) = \min F(B, H, t, \mathbf{A}, \mathbf{N}) = \min \left(A_x(B, H, t) L_D + P_s \sum_{i=1}^{n_s} A_i L_{s,i} \right), \tag{1}$$

where the set of design variables $\mathbf{x}$ consists of the deck shape variables (the width B and the depth H of the deck cross-section), the deck plate thickness t, and the stays cross-section areas $\mathbf{A} = \left| A_1, \ldots, A_{n_s} \right|$, and prestressing forces $\mathbf{N} = \left| N_1, \ldots, N_{n_s} \right|$, where n_s is the number of stays. P_s is the number of planes of stays, which in the case of long-span bridges is commonly 2. In this manner, the objective function provides the volume of the deck and stays, which is the quantity to minimize. The structural and aeroelastic constraints ($g_i(\mathbf{x}) < 0$) are the following:

1. Maximum displacements allowed in the deck and tower under self weight (SW). These limits are applied to the vertical displacements of the deck w^D and the horizontal displacements of the top of the towers u^T. These constraints are formulated as:

$$g_d^{w^D, SW}(\mathbf{x}) = \frac{w_d^{D, SW}}{w_{\max}^{D, SW}} - 1 \leq 0, \quad d = 1, \ldots, n_d, \tag{2}$$

$$g_t^{u^T, SW}(\mathbf{x}) = \frac{u_t^{T, SW}}{u_{\max}^{T, SW}} - 1 \leq 0, \quad t = 1, \ldots, n_t, \tag{3}$$

where $g_d^{w^D, SW}(\mathbf{x})$ are the constraints imposed to the vertical displacements of the center of the deck at the n_d longitudinal locations of the stays' anchorages at the deck, and $g_t^{u^T, SW}(\mathbf{x})$ are the n_t constraints for the horizontal displacements of the top of the towers at points t. These constraints are established to obtain the prestressing forces during the optimization process, as developed in Baldomir et al. [19].

2. Maximum displacements allowed in the deck and towers under different distributions L_l of n_l live loads. The formulation of these constraints, which are imposed in the same control points and degree-of-freedom (DoF) used in Eqs. (2) and (3), can be written as:

$$g_d^{w^D, L_l}(\mathbf{x}) = \frac{w_d^{D, L_l}}{w_{\max}^{D, L_l}} - 1 \leq 0, \quad d = 1, \ldots, n_d, \quad l = 1, \ldots, n_l, \tag{4}$$

$$g_t^{u^T, L_l}(\mathbf{x}) = \frac{u_t^{T, L_l}}{u_{\max}^{T, L_l}} - 1 \leq 0, \quad t = 1, \ldots, n_t, \quad l = 1, \ldots, n_l. \tag{5}$$

Table 1
Natural frequencies and modal shapes for the initial and optimum structural design considering the baseline G1 deck cross-section (initial deck shape design).

Φ shape[a]	Initial design		Optimum design (G1)	
	Mode #	$f_{n,0}$ [Hz]	Mode #	f_n^* [Hz]
L1s	**1**	0.082	**1**	0.080
Towers & L2a	2	0.154	2	0.155
Towers & L1s	3	0.155	3	0.155
Long.	4	0.194	4	0.198
V1s	**5**	0.203	**5**	0.213
L2a	6	0.231	6	0.232
V2a	7	0.255	7	0.242
V3s	**8**	0.351	**8**	0.349
V4al	9	0.411	9	0.354
L3s & T1s	**10**	0.419	**11**[b]	0.414
V5s[c]	**11**	0.438	**10**[b]	0.367
T1s	**12**	0.461	**12**	0.449
L4al	13	0.489	14[b]	0.490
V4a	14	0.496	13[b]	0.474
V5s	**15**	0.518	**15**	0.490
L3s & T1s	**16**	0.533	**16**	0.530
V7s[d]	17	0.622	18[b]	0.578
V6a	18	0.631	17[b]	0.569
V7sl	19	0.682	19	0.597
L4s & T2a	20	0.700	21[b]	0.696
V6al	21	0.705	20[b]	0.637
Towers & L3s	22	0.726	22	0.724

[a] L = lateral, V = vertical, T = torsional, # = number of half-waves in the mode shape of the main span, s = symmetric shape, a = asymmetric shape, & = combination of shapes, l = strong vertical displacement in the side spans. The modes with higher influence on the buffeting responses are indicated in bolt.
[b] This mode has a different position on the frequency list with regards to the initial design of the bridge.
[c] The shape of the optimum design is "V5s" although the first and fifth half-waves are almost inappreciable in Fig. 4.
[d] The shape of the initial design is "V5s" and the shape of the optimum design is "V7s", as shown in Fig. 4.

Table 2
Summary of maximum acceleration limits for buffeting response found in the literature. Values of RMS of accelerations in m/s^2. The torsional accelerations are expressed as the equivalent vertical accelerations of the deck according to $Z_{eq} = \theta \cdot B/2$.

Source	U range [m/s]	$\ddot{u}_{RMS,max}$	$\ddot{w}_{RMS,max}$	$\ddot{Z}_{eq,RMS,max}$
Stretto di Messina [48]	[5 − 40]	0.150	0.250	0.125
	[40 − ∞]	0.300	0.500	0.250
ISO 2631 [45]	[0 − 15]	0.200	0.200	0.200
	[15 − ∞]	0.500	0.500	0.500

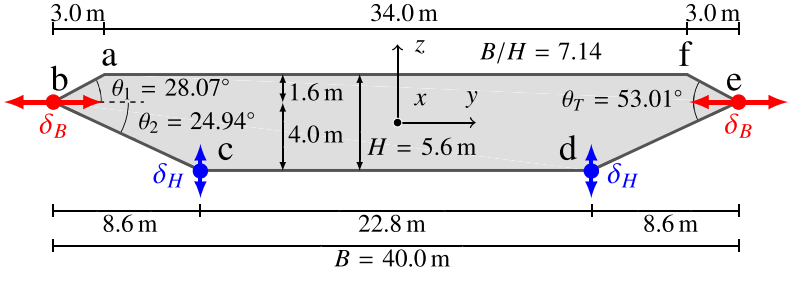

Fig. 3. Baseline G1 Scanlan's cross-section and the deck shape variables δ_B and δ_H.

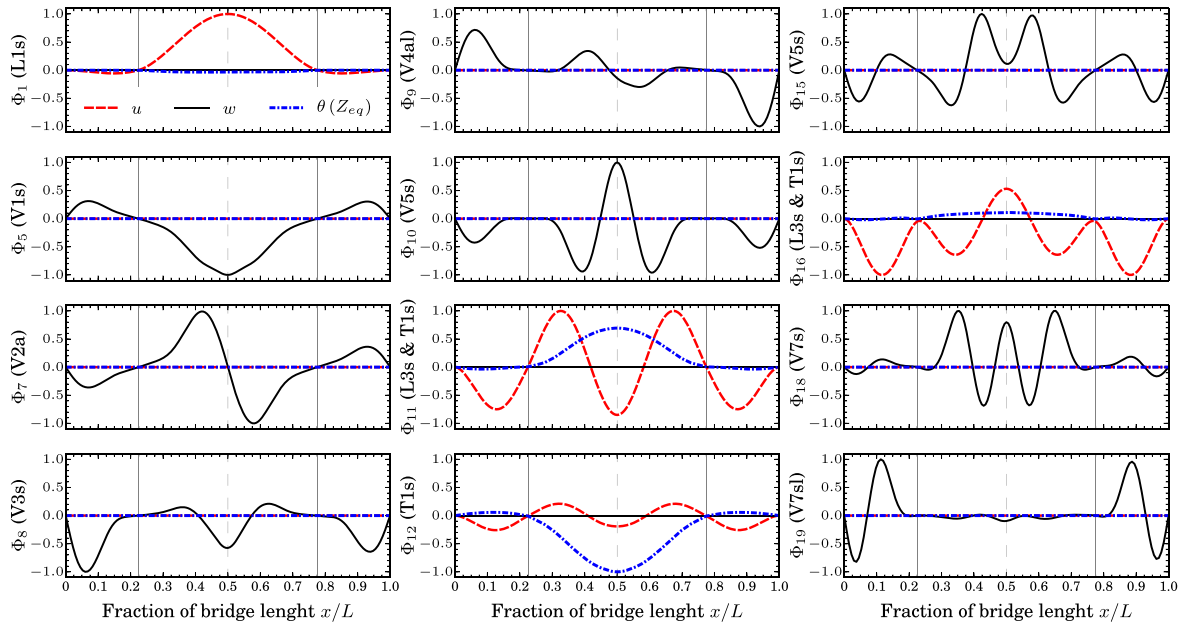

Fig. 4. Mode shapes of the deck normalized to displacements of the optimum structural design considering the G1 cross-section. Torsional DoF of the modes are expressed as $Z_{eq} = \theta \cdot B/2$. Natural frequencies and modes numeration can be found in Table 1. The location of the towers is indicated by a gray line and the center of the main span can be identified by a dashed gray line.

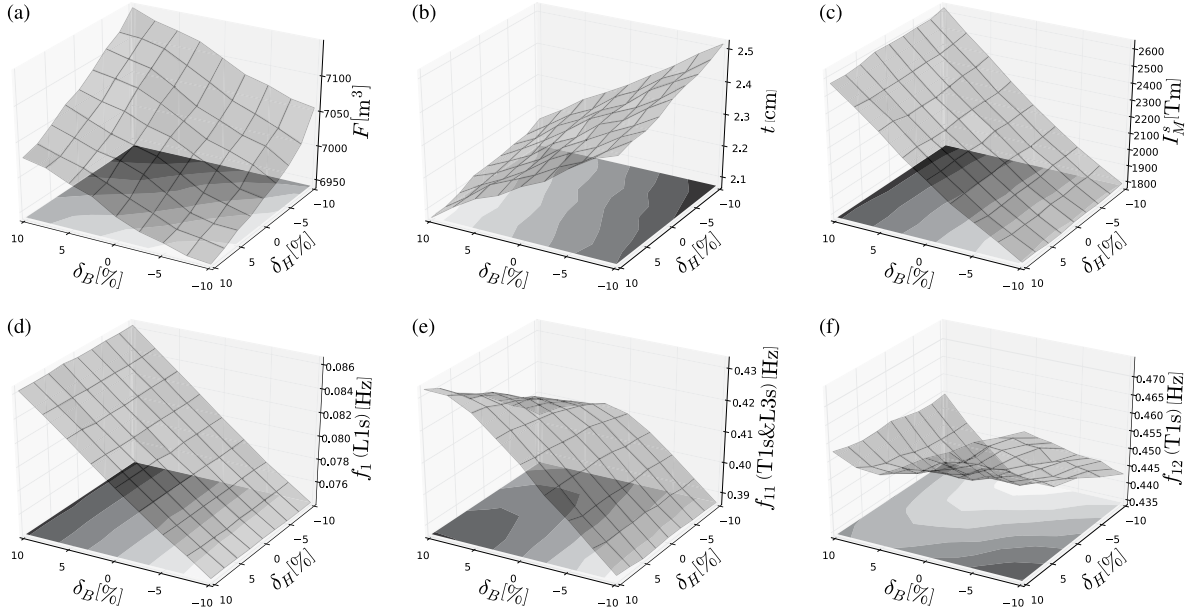

Fig. 5. Response surfaces of a subset of relevant properties on the optimum shape space S^*: (a) objective function F (Eq. (1)), (b) deck plate thickness t, (c) structural mass moment I_M^S, (d) natural frequency of mode #1, (e) natural frequency of mode #11, and (f) natural frequency of mode #12 (see Table 1).

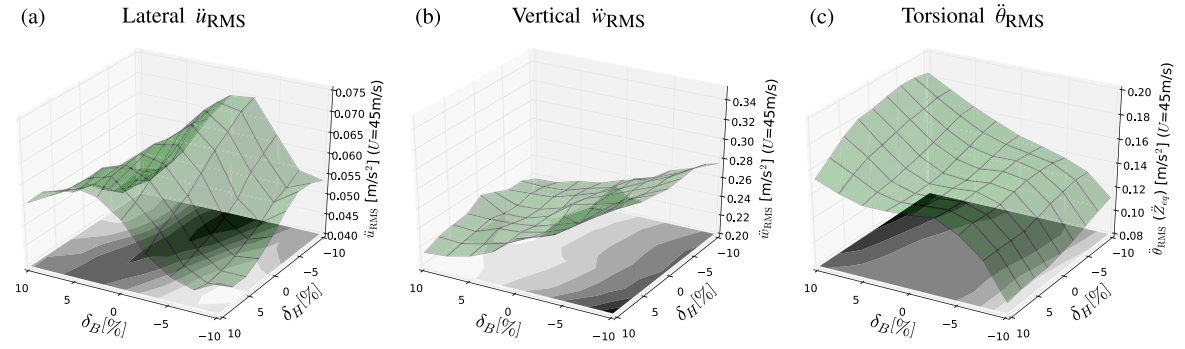

Fig. 6. BARS for the optimum designs in S^* at wind speed $U = 45$ m/s in terms of RMS of accelerations at midspan in m/s^2. The torsional accelerations are expressed as the equivalent vertical accelerations of the deck according to $Z_{eq} = \theta \cdot B/2$.

Table 3
Initial values ($\mathbf{x}_0$), lower bounds ($\mathbf{x}_{min}$), and upper bounds ($\mathbf{x}_{max}$) of the design variables ($\mathbf{x}$) considered for the aero-structural shape optimization, which are the deck width B and depth H, the deck thickness t, the area of the stays $\mathbf{A}$ (this includes the backstays area $\mathbf{A}^B$ and the area of the other stays $\mathbf{A}^s$) and the prestressing forces of the stays $\mathbf{N}$.

Type	Design variable	# variables	$\mathbf{x}_0$	$\mathbf{x}_{min}$	$\mathbf{x}_{max}$
Shape	B [m]	1	40.0	36.0	44.0
	H [m]	1	5.6	5.04	6.16
Size	t [cm]	1	2.5	1.0	3.0
	$\mathbf{A}^B$ [m^2]	2	0.5	0.0033	1.0
	$\mathbf{A}^s$ [m^2]	38	0.05	0.0033	1.0
Other	$\mathbf{N}$ [MPa]	40	300	0.0	800[a]

[a]This value is directly conditioned by Eqs. (8) and (9).

3. Maximum normal stresses allowed at the top and bottom fibers of the deck cross section for the n_l distributions of the live loads. The constraints are given by:

$$g_k^{\sigma^{TF,L_l}}(\mathbf{x}) = \frac{\sigma_k^{TF,L_l}}{\sigma_{\max}^{TF,L_l}} - 1 \leq 0, \quad k = 1,\dots,n_k, \quad l = 1,\dots,n_l, \tag{6}$$

$$g_k^{\sigma^{BF,L_l}}(\mathbf{x}) = \frac{\sigma_k^{BF,L_l}}{\sigma_{\max}^{BF,L_l}} - 1 \leq 0, \quad k = 1,\dots,n_k, \quad l = 1,\dots,n_l, \tag{7}$$

where n_k is the number of control points along the deck at which this design constraint is evaluated, σ^{TF} is the stress at the top fiber of the deck cross-section and σ^{BF} represents the stress at the deck bottom fiber. These values can be obtained from the deck axial load and bending moments in a FEM based on beam and bar elements.

4. Maximum normal stress allowed in the stays for the live loads and self-weight load case. This constraint is applied to the n_s stays for each load case (SW and L_l), and is written as:

$$g_i^{\sigma^{s,L_l}}(\mathbf{x}) = \frac{\sigma_i^{s,L_l}}{\sigma_{\max}^{s,L_l}} - 1 \leq 0, \quad i = 1,\dots,n_s, \quad l = 1,\dots,n_l, \tag{8}$$

$$g_i^{\sigma^{s,SW}}(\mathbf{x}) = \frac{\sigma_i^{s,SW}}{\sigma_{\max}^{s,SW}} - 1 \leq 0, \quad i = 1,\dots,n_s, \tag{9}$$

where σ_i^s is the stress at each stay i, including the backstays.

5. Maximum allowed RMS of accelerations along the deck due to buffeting loads. The n_j buffeting control points are uniformly distributed along the deck. These constraints must be formulated for all the n_h wind velocities considered and the three DoF as:

$$g^{\ddot{u}_{RMS}}(\mathbf{x}) = \frac{\ddot{u}_{RMS,j}^{U_h}}{\ddot{u}_{RMS,j,max}^{U_h}} - 1 \leq 0, \quad j = 1,\dots,n_j, \quad h = 1,\dots,n_h, \tag{10}$$

$$g^{\ddot{w}_{RMS}}(\mathbf{x}) = \frac{\ddot{w}_{RMS,j}^{U_h}}{\ddot{w}_{RMS,j,max}^{U_h}} - 1 \leq 0, \quad j = 1,\dots,n_j, \quad h = 1,\dots,n_h, \tag{11}$$

$$g^{\ddot{\theta}_{RMS}}(\mathbf{x}) = \frac{\ddot{\theta}_{RMS,j}^{U_h}}{\ddot{\theta}_{RMS,j,max}^{U_h}} - 1 \leq 0, \quad j = 1,\dots,n_j, \quad h = 1,\dots,n_h, \tag{12}$$

where $\ddot{u}_{RMS,j}^{U_h}$, $\ddot{w}_{RMS,j}^{U_h}$ and $\ddot{\theta}_{RMS,j}^{U_h}$ are the RMS of lateral, vertical and torsional accelerations of the bridge deck, respectively, obtained following the procedure described in Section 2 and using the multi-mode frequency domain approach (Scanlan [60] and Diana et al. [61]). It must be noted that while in flutter-resistant design optimization frameworks the aeroelastic response is limited by the minimum flutter velocity, here the threshold is the maximum allowed RMS of accelerations for each DoF, control point, and wind velocity ($\ddot{u}_{RMS,j,max}^{U_h}$, $\ddot{w}_{RMS,j,max}^{U_h}$ and $\ddot{\theta}_{RMS,j,max}^{U_h}$), leading to a relevant number of aeroelastic design constraints.

The maximum values adopted as bounds for each constraint are identified with the subindex max. The values taken for those limits, which are based on codes and/or engineering practice criteria, are provided in Section 6.1. The design variables associated with the stays' cross-sections areas take the values of the inverse areas of the stays ($1/A_i$), aiming at easing the convergence of the optimization problem (see Eqs. (8) and (9) and Vanderplaats and Salajegheh [62]).

4. Description of the application case

The single-box long-span bridge used as an application example in this study is the same as the one adopted in Cid Montoya et al. [57] to facilitate the interpretation of the results. A detailed description of the model, the turbulent wind conditions, and the procedure adopted for the buffeting analyses can be found in that reference. A short description is presented here for completeness.

The cable-stayed bridge has a main span of 1316 m and two side spans of 540 m, which is in the order of magnitude of the Russky or Sutong bridges. The FEM of the structure is sketched in Fig. 2. The deck cross-section is the well-known Scanlan's G1 section (Scanlan and Tomko [63]), similar to the deck cross-section of the main span of the Great Belt Bridge and described in Fig. 3, where the deck shape variables, width B and depth H, are defined in terms of their relative variation δ_B and δ_H, respectively. A maximum variation of $\pm 10\%$ is enabled for both shape design variables, resulting in geometries with B/H ratios ranging from 5.84 to 8.73, and fairing angles θ_T between 35.70° to 92.63°. The aerodynamic response of the deck cross-sections included in the shape design domain is obtained from a surrogate model developed in Cid Montoya et al. [37]. In that study, the accuracy of the force coefficients obtained by 2D URANS CFD simulations, the performance of the QS formulation in estimating the flutter derivatives, and the accuracy of the full surrogate-based numerical procedure to assess the flutter velocity as a function of the deck shape were successfully validated using experimental data obtained from sectional model wind tunnel tests of three different deck geometries. The Kriging surrogate has two inputs, which are the deck shape variables H and B, and six outputs, namely the three force coefficients and their slopes that are required to apply the quasi-steady theory to estimate the flutter derivatives and admittance function. The surrogate model was built from 15 samples consisting of CFD simulations using 2D URANS and Menter's $k-\omega$ SST turbulence model that provides the force coefficients at wind angles of attack $\alpha = 0°$ and $\alpha = 2°$. This information can be used to calculate the slopes of the force coefficients at $\alpha = 0°$ of streamlined deck cross-sections.

5. Buffeting response of the optimum structural bridge design configuration

The buffeting responses of the optimum structural designs are studied in this section in order to be later used to interpret the optimum aero-structural designs that will be reported in Section 6.

5.1. Structural optimization problem

The structural optimization problem is formulated as outlined in Section 3, without considering the buffeting constraints (Eqs. (10) to (12)), and assuming that the shape design variables that define the geometry of the deck cross-section (B and H) are fixed. Consequently,

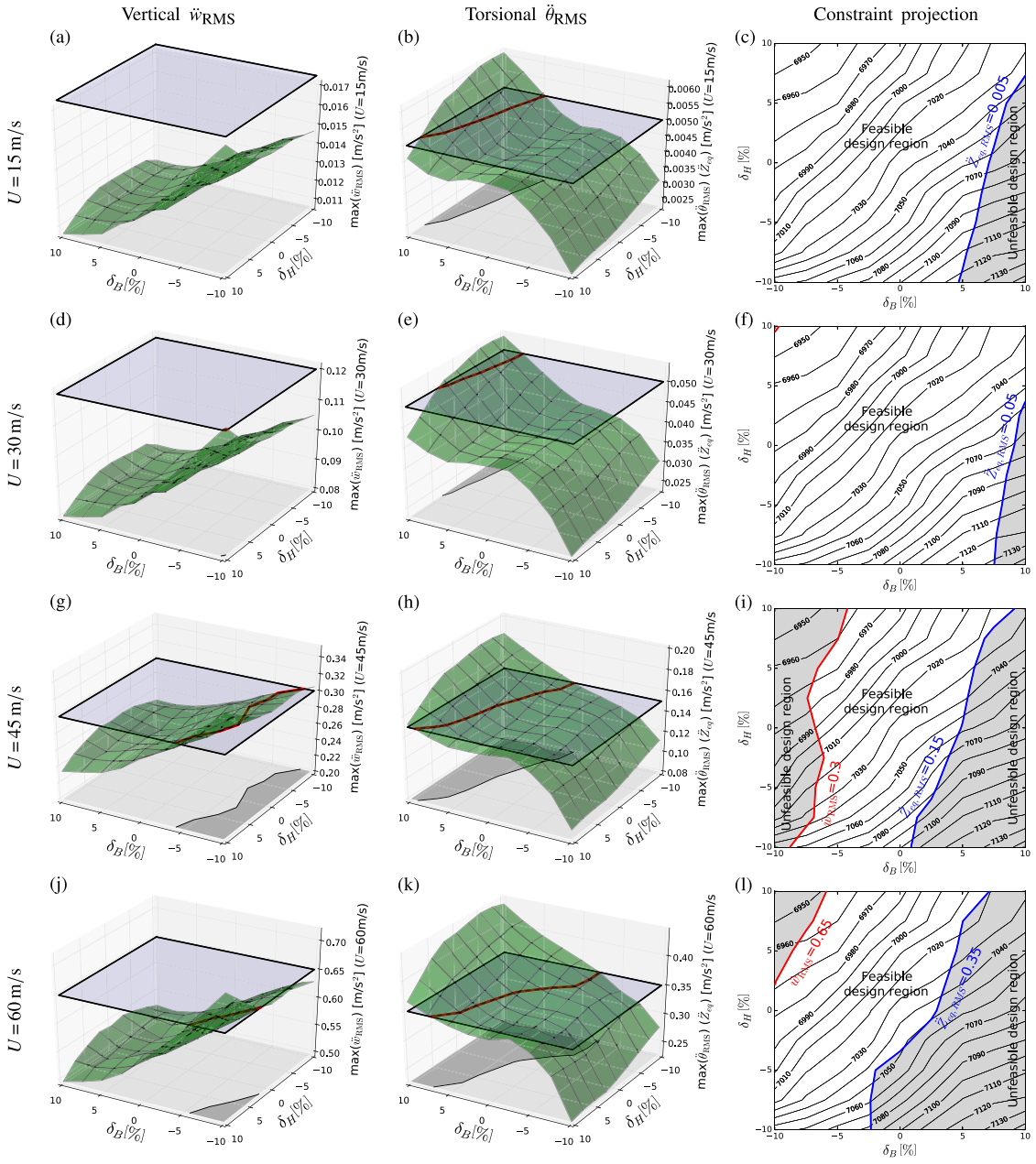

Fig. 7. BARS of the maximum responses for the optimum designs in S^* at wind speed $U = [15, 30, 45, 60]$ m/s compared with a set of limits defined in Section 5.4 for each constraint. On the right side (c, f, i, and l), the related constraints as formulated in Eqs. (10) to (12) are projected over S^*, along with the values of the objective function F (Eq. (1)). (For interpretation of the references to color in this figure legend, the reader is referred to the web version of this article.)

the formulation of the objective function can be rewritten for the structural optimization problem as

$$\min F(t, \mathbf{A}, \mathbf{N}) = A_x(t) L_D + P_s \sum_{i=1}^{40} A_i L_{s,i}, \tag{13}$$

subject to

$$g_r^{Str}(\mathbf{x}) = \frac{R_r}{R_{r,\max}} - 1 \leq 0, \quad r = 1, \ldots, 1104. \tag{14}$$

where g_r^{Str} represents all the structural design constraints included in Eqs, (2) to (9), being r the number of each structural constraint, R_r the structural response and $R_{r,\max}$ the maximum value allowed for each response.

5.2. Optimum shape design space S^*

The structural optimization problem defined above makes it possible to obtain, for a given deck shape geometry (fixed values of the deck shape variables B and H), the optimum structural values of the other design variables t, $\mathbf{A}$ and $\mathbf{N}$. This approach can be applied to any deck shape geometry included in the shape design space S, namely the design domain involving the shape design variables and their lower and upper bounds. The result of this procedure is a new design space composed by the optimum values of the design variables t^*, $\mathbf{A}^*$ and $\mathbf{N}^*$ for each pair of values of B and H, which is defined as optimum shape design space S^* (Cid Montoya et al. [38]). Therefore, the responses of the structural optimum bridge as a function of the shape design variables B and H can be represented in this new design space. Note that the symbol *, when referred to any property or design variable

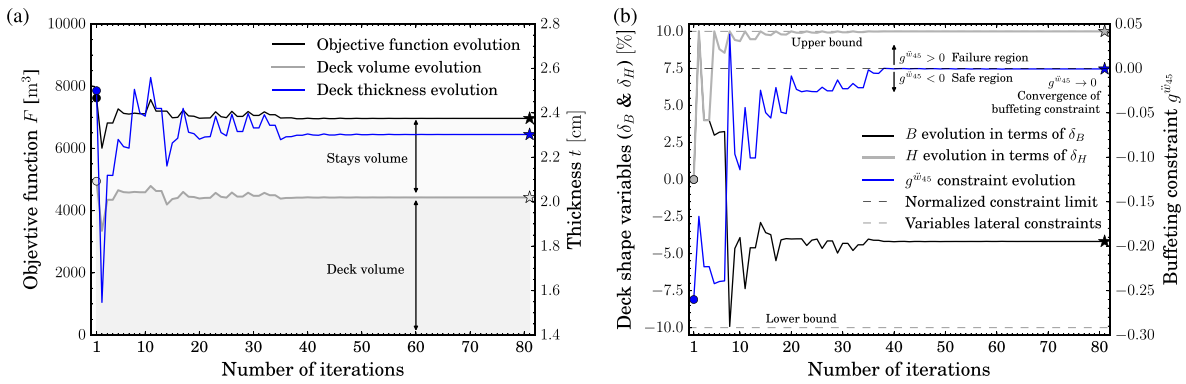

Fig. 8. Evolution of relevant parameters in the optimization process: (a) objective function F (Eq. (1)) and deck thickness t; and (b) deck width B and depth H, and the active buffeting constraint $g^{\ddot{w}_{45}}$ (RMS of vertical accelerations at wind velocity $U = 45$ m/s, see Eq. (11)). (For interpretation of the references to color in this figure legend, the reader is referred to the web version of this article.)

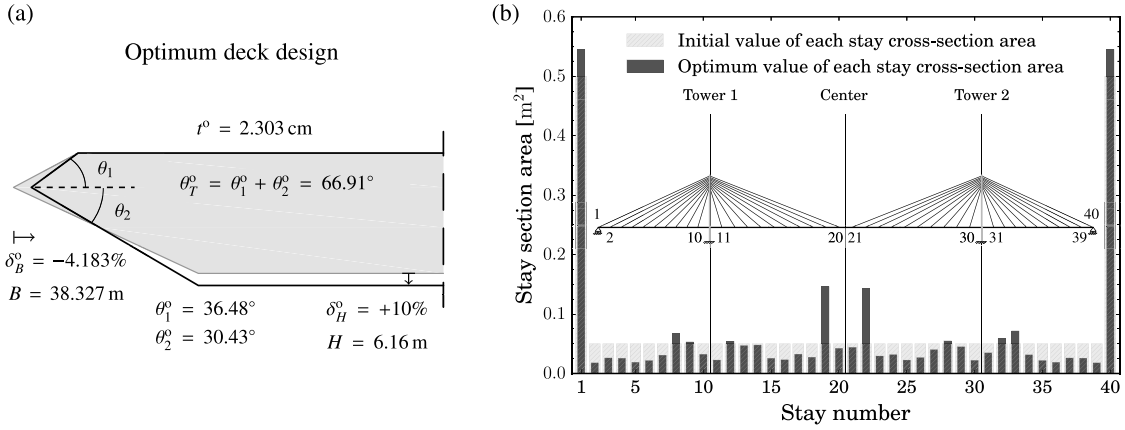

Fig. 9. Optimum bridge design: (a) initial (gray) and optimum (black) deck shape and size design; and (b) initial and optimum design of the cross-section area of each stay.

of the bridge design, denotes the result of the structural optimization process, or in other words, the optimum structural design.

5.3. Dynamic responses of the bridge over S^*

The natural frequencies of the initial and optimum structural design considering the G1 baseline deck cross-section ($B = 40$ m and $H = 5.6$ m, see Section 4) are shown in Table 1, while the mode shapes of the optimum are plotted in Fig. 4.

Fig. 5 shows a subset of response surfaces of relevant properties over S^*, including the objective function F, the deck plate thickness t, the structural mass moment of inertia I_M^s, and three representative natural frequencies: the first lateral mode f_1 "L1s", and the most relevant torsional modes f_{11} "T1s & L3s" and f_{12} "T1s" (see Fig. 4).

5.4. Buffeting responses over S^*: Interpretation from the designer's perspective

The influence of the deck shape on the buffeting response is analyzed in this Section. Buffeting responses are represented as response surfaces as a function of the deck shape, defined as buffeting acceleration response surface (BARS). These responses in S^* are the ones that the optimization algorithm will find in the last stages of the convergence process when approaching the neighborhood of the optimum design. Therefore, they can be used to interpret the optimum designs obtained and the design decisions taken by the optimization algorithm in the complete aero-structural optimization problem, particularly for the shape design variables B and H.

Fig. 6 shows the accelerations of the three DoF at midspan along with the maximum acceleration found along the deck for each DoF. It must be remarked the sensitivity of the buffeting response with the deck width B, as it was reported in detail in Cid Montoya et al. [57] for the initial design of the bridge. Similar tendencies are found here in S^*, where the vertical accelerations are higher for narrow decks, while wider deck designs produce higher torsional accelerations. On the other hand, the lateral accelerations are irrelevant in the chosen design domain.

Finding the area of the design domain where the responses surpass the values adopted as the maximum allowed accelerations permits the identification of the feasible and unfeasible domain regions. The limit values adopted for the buffeting accelerations were selected based on information found in the literature. A relevant source is the International Organization for Standardization (ISO), particularly the code ISO 2631 [45], where maximum accelerations for human discomfort are provided. Also, in the specifications for the Messina Strait Bridge (Stretto di Messina [48]), a set of requirements to verify the stress and fatigue strength of the deck members were set for buffeting accelerations under turbulent winds characterized in terms of turbulence intensity as $I_u = 7\%$, $I_v = 0.75 I_u$ and $I_w = 0.50 I_u$. All these requirements are summarized in Table 2.

Hence, the limit values adopted are $\ddot{u}_{RMS,max}(U) = [0.005, 0.04, 0.15, 0.30]$ m/s^2 for the lateral accelerations, $\ddot{w}_{RMS,max}(U) = [0.0175, 0.12, 0.3, 0.65]$ m/s^2 for the vertical response, and for the torsional response $\ddot{Z}_{eq,RMS,max}(U) = [0.005, 0.05, 0.15, 0.35]$ m/s^2. These limit values adopted for the buffeting accelerations correspond to the following wind intervals: $U_1 = [0 - 15]$ m/s, $U_2 = [15 - 30]$ m/s, $U_3 = [30 - 45]$ m/s and $U_4 = [45 - 60]$ m/s. The buffeting responses are calculated for the maximum velocity of each range $U = [15, 30, 45, 60]$ m/s

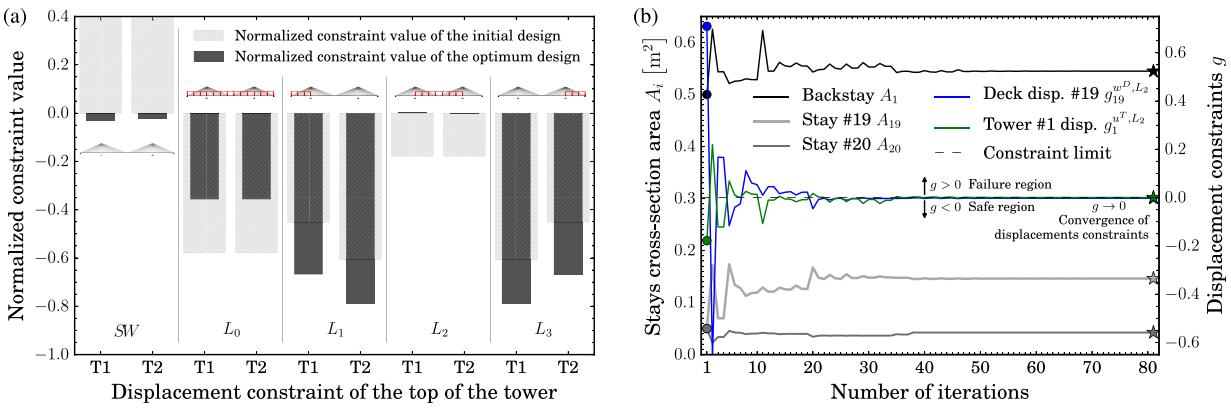

Fig. 10. Subset of displacement design constraints: (a) shows all the constraint of top of the tower for several load cases (Eqs. (3) and (5)); and (b) compares the convergence of three relevant stays area and the displacements design constraints of the tower and the deck and midspan. (For interpretation of the references to color in this figure legend, the reader is referred to the web version of this article.)

Table 4
Summary of design constraints considered in the aero-structural optimization problem.

Type	Location	Limit constraint value	# RP[a]	Load cases[b]	# constraints
Displacement under self weigth	Deck nodes	$w_{\max} = 0.05$ m	38	SW (1)	38
	Tower top nodes	$u_{\max} = 0.05$ m	2	SW (1)	2
Displacement under live loads	Lateral spans	$w_{\max} = 540$ m / 500 = 1.080 m	18	L (4)	72
	Main span	$w_{\max} = 1316$ m / 500 = 2.632 m	20	L (4)	80
	Tower top nodes[c]	$u_{\max} = 314.4$ m / 600 = 0.524 m	2	L (4)	8
Stress under self weight and live loads	Deck top fiber	$\sigma_{\max} = 200$ MPa	88	L (4)	352
	Deck bottom fiber	$\sigma_{\max} = 200$ MPa	88	L (4)	352
	Stays	$\sigma_{\max} = 800$ MPa	40	$SW\&L$ (5)	200
Buffeting loads: RMS of acceleration	Deck lateral accel.	$\ddot{u}_{RMS}^{\max}(U) = [0.005, 0.04, 0.15, 0.30]$ m/s^2	171	B_U (4)	684
	Deck vertical accel.	$\ddot{w}_{RMS}^{\max}(U) = [0.0175, 0.12, 0.3, 0.65]$ m/s^2	171	B_U (4)	684
	Deck torsional accel.	$\ddot{Z}_{eq\,RMS}^{\max}(U) = [0.005, 0.05, 0.15, 0.35]$ m/s^2	171	B_U (4)	684
Total number of design constraints				$SW\&L\&B_U$	3156

[a] RP = Response points where the response of the bridge is controlled by a design constraint.
[b] SW = self weight, L = live loads, B_U = buffeting loads for each wind velocity value U, (#) = total number of load cases.
[c] The height of the tower used in this constraint is related to the location of the backstay anchorage, which is 3 m below the top of the tower.

and are checked against the maximum accelerations allowed for each wind velocity.

Fig. 7 shows the whole picture of the buffeting accelerations design constraints for the set of wind velocities under study $U = [15, 30, 45, 60]$ m/s. In this figure, the values shown are the maximum RMS of accelerations along the entire deck. They are represented along with the values of the objective function F (Eq. (1)) obtained in S^* (see Fig. 5). Since lateral constraints are not active (see the low values reported in Fig. 6), only vertical and torsional responses are shown. The constraints projections over the design domain are plotted in Fig. 7 (c), (f), (i), and (l) for each wind velocity U. It is worth noting that the constraints for low values of wind velocity, namely $U = [15, 30]$ m/s, do not significantly reduce the feasible design region, which only is constrained by the torsional response for high values of B. For cases $U = [45, 60]$ m/s, both vertical and torsional responses limit the feasible design domain, being the case $U = 45$ m/s the most restrictive one, although the case $U = 60$ m/s is more demanding for low values of H. In general, the vertical acceleration design constraint bounds the feasible design domain for low values of B, while the torsional design constraint prevents designs with large values of B.

The opposite trends in the vertical and torsional buffeting responses as a function of B and also H, lead to a trade-off situation in terms of design decisions, according to the values adopted as limits for the design constraints. Also, the desired goal of reducing the objective function F (Eq. (1)), leads to another trade-off between these constraints and F, which highlights the need for adopting optimization procedures to find the most efficient design.

6. Aero-structural optimization of the bridge considering shape and size design variables

6.1. Definition of the problem

The formulation of the aero-structural optimization problem has been presented in Section 3 and the application case was briefly introduced in Section 4. The initial design of the design variables and the limits of their lateral constraints, namely lower and upper bounds, are given in Table 3, and all information related to the constraints are provided in Table 4. This table classifies the different design constraints, provides the limit values, and indicates the number of response points used for each constraint. It can be noted that there are three groups of response points distributed along the deck: a set of 38 points at the location of the stays anchorages used to control the deck displacements (see Eq. (2)), a set of 88 control points to check the stress levels along the deck (Eqs. (6) and (7)), and another set of 171 response points uniformly distributed to evaluate the RMS of accelerations at four wind velocities (Eqs. (10) to (12)). The set of gravitational load cases includes the self weight (SW) of the structure and four live load cases ($L_l, l = 0, \ldots, 3$) to model some arrangements of service traffic loads on the deck. These live loads are modeled by a uniformly distributed load of 136 kN/m along the whole bridge in the first case (L_0), and along the left, center, and right spans in the second (L_1), third (L_2), and fourth (L_3) cases, respectively. The limit values adopted for the buffeting accelerations were discussed in Section 5.4 and are also summarized in Table 4.

Table 5
Initial and optimum designs obtained by the aero-structural optimization.

	Property	Design		Variation	
		Initial	Optimum	Δ	δ [%]
General	Objective function F [m^3]	7619.200	6964.178	655.022	8.597
	Volume of stays V^s [m^3]	2673.290	2540.198	133.092	4.979
	Percentage of stays in F [%]	35.086	36.480	1.394	3.973
	Volume of deck V^D [m^3]	4945.910	4423.980	521.930	10.553
	Percentage of deck in F [%]	64.914	63.520	1.394	2.147
Stays	Backstays mean area $\tilde{A}^B$ [m^2]	0.500	0.545	0.045	9.000
	Stays mean area $\tilde{A}^s$ [m^2]	0.050	0.040	0.010	19.400
	Backstay/Stay area ratio	10.000	13.524	3.524	35.236
	Mean area of all stays [m^2]	0.073	0.066	0.007	10.274
	Mean prestressing force $\tilde{N}$ [MPa]	300.000	475.500	175.500	58.500
Deck[d]	Width B [m]	40.000	38.327	1.673	4.183
	Depth H [m]	5.600	6.160	0.560	10.000
	Plate thickness t [cm]	2.500	2.303	0.197	7.880
	A_x [m^2]	2.064	1.846	0.218	10.562
	J_x [m^4]	41.360	44.679	3.319	8.025
	I_y [m^4]	12.516	13.761	1.245	9.947
	I_z [m^4]	288.176	239.116	49.060	17.024
	Structural weight M_x^S per m. [T/m]	16.101	14.399	1.702	10.572
	Total weight M_x per m. [T/m]	24.101	22.399	1.702	7.063
	Live load/Weight ratio	0.576	0.620	0.044	7.600
	Structural mass moment $I^S_{M_x}$ per m. [Tm/m]	2345.398	1972.661	372.737	15.892
	Total mass moment I_{M_x} per m. [Tm/m]	4645.398	4272.661	372.737	8.024
Dynamics[f]	f_1 (L1s) [Hz]	0.082	0.078	0.004	4.878
	f_5 (V1s) [Hz]	0.203	0.214	0.011	5.419
	f_8 (V3s) [Hz]	0.351	0.355	0.004	1.140
	f_{10} (L3s & T1s) [Hz]	0.419	0.404	0.015	3.580
	f_{11} (V5s) [Hz]	0.438	0.377	0.061	13.927
	f_{12} (T1s) [Hz]	0.461	0.468	0.007	1.518
	f_{15} (V5s) [Hz]	0.518	0.495	0.023	4.440
	f_{16} (L3s & T1s) [Hz]	0.533	0.513	0.020	3.752
	f_{17} (V5s) [Hz]	0.622	0.608	0.014	2.251
Buffeting[s,a]	$\max(\ddot{u}_{\text{RMS}})$ [m/s^2] (U = 15 m/s)	0.0022[s86]	0.0019[s86]	0.0003	12.542
	$\max(\ddot{u}_{\text{RMS}})$ [m/s^2] (U = 30 m/s)	0.0175[s86]	0.0144[s86]	0.0030	17.427
	$\max(\ddot{u}_{\text{RMS}})$ [m/s^2] (U = 45 m/s)	0.0604[s86]	0.0468[s86]	0.0135	22.441
	$\max(\ddot{u}_{\text{RMS}})$ [m/s^2] (U = 60 m/s)	0.1492[s56]	0.1121[s86]	0.0371	24.859
	$\max(\ddot{w}_{\text{RMS}})$ [m/s^2] (U = 15 m/s)	0.0127[s82]	0.0143[s9]	0.0016	12.662
	$\max(\ddot{w}_{\text{RMS}})$ [m/s^2] (U = 30 m/s)	0.0909[s81]	0.1033[s9]	0.0124	13.681
	$\max(\ddot{w}_{\text{RMS}})$ [m/s^2] (U = 45 m/s)	0.2525[s81]	**0.2999**[s9]	0.0474	18.750
	$\max(\ddot{w}_{\text{RMS}})$ [m/s^2] (U = 60 m/s)	0.4872[s79]	0.6246[s8]	0.1374	28.202
	$\max(\ddot{\theta}_{\text{RMS}})$ ($\ddot{Z}_{eq}$) [m/s^2] (U = 15 m/s)	0.0044[s86]	0.0040[s86]	0.0003	7.835
	$\max(\ddot{\theta}_{\text{RMS}})$ ($\ddot{Z}_{eq}$) [m/s^2] (U = 30 m/s)	0.0403[s86]	0.0382[s86]	0.0021	5.303
	$\max(\ddot{\theta}_{\text{RMS}})$ ($\ddot{Z}_{eq}$) [m/s^2] (U = 45 m/s)	0.1420[s86]	0.1377[s86]	0.0043	3.043
	$\max(\ddot{\theta}_{\text{RMS}})$ ($\ddot{Z}_{eq}$) [m/s^2] (U = 60 m/s)	0.3342[s86]	0.3338[s86]	0.0005	0.139

[f] The identificative number of the frequencies shown in this table are the numbers reported in Table 1.
[d] The properties given for the deck are per unit of length (meter).
[s] The sections or control points where the maximum buffeting response is found along the deck are indicated for each response. Only the section number on the left side of the bridge is provided for simplicity. Note that midspan correspond to section #86, since 171 control points are considered.
[a] The buffeting active constraint is indicated in bolt. Note that the active section is #163, the symmetric control point of #9 (see Fig. 12 (d)).

6.2. Optimization results

This section reports the results of the aero-structural optimization design problem considering the set of constraints described in Table 4. The modifications carried out by the optimization algorithm are summarized in Table 5, where the properties of the initial design are compared with the ones of the optimum design, and the relative and absolute variations are provided. Also, a summary of the variations of the main design variables, properties and design constraints of the bridge are reported in Figs. 8 to 12. The optimization algorithm has been able to reduce the amount of material of the bridge, namely the objective function F, by 8.6%, which would allow a noticeable reduction in terms of the economic cost of the structure. This was achieved mainly by the reduction in the volume of the deck, finding a more efficient deck shape that enables the reduction of the deck plate thickness. The convergence of the objective function along the optimization process is given in Fig. 8 (a), where the distribution of material between the deck and the stays is indicated. It can be noted in this figure the important role played by the deck thickness in the objective function value along the optimization process.

Fig. 9 summarizes the changes adopted for the shape and size design variables. It can be seen that the depth of the deck cross-section is increased to the upper bound, given its important contribution to the stiffness properties of the deck girder, and the optimum deck is slightly less wide. This deck design keeps the aeroelastic responses below the design threshold as shown in Fig. 8 (b) for the RMS of vertical accelerations. The cross-section area of most of the stays of the bridge is reduced, and the uniform distribution of cross-section area adopted in the initial design is modified, providing more efficient distribution of cross-section areas, as shown in Fig. 9. The cross-section area of the backstays and the stays next to the main span is increased, given the important role played by these stays to improve the performance of the bridge against gravitational loads. This is shown in Fig. 10 (b), where the convergence of the cross-section area of three relevant stays are compared with the structural design constraints related to the horizontal displacement at the top of the tower and the vertical displacements of the deck.

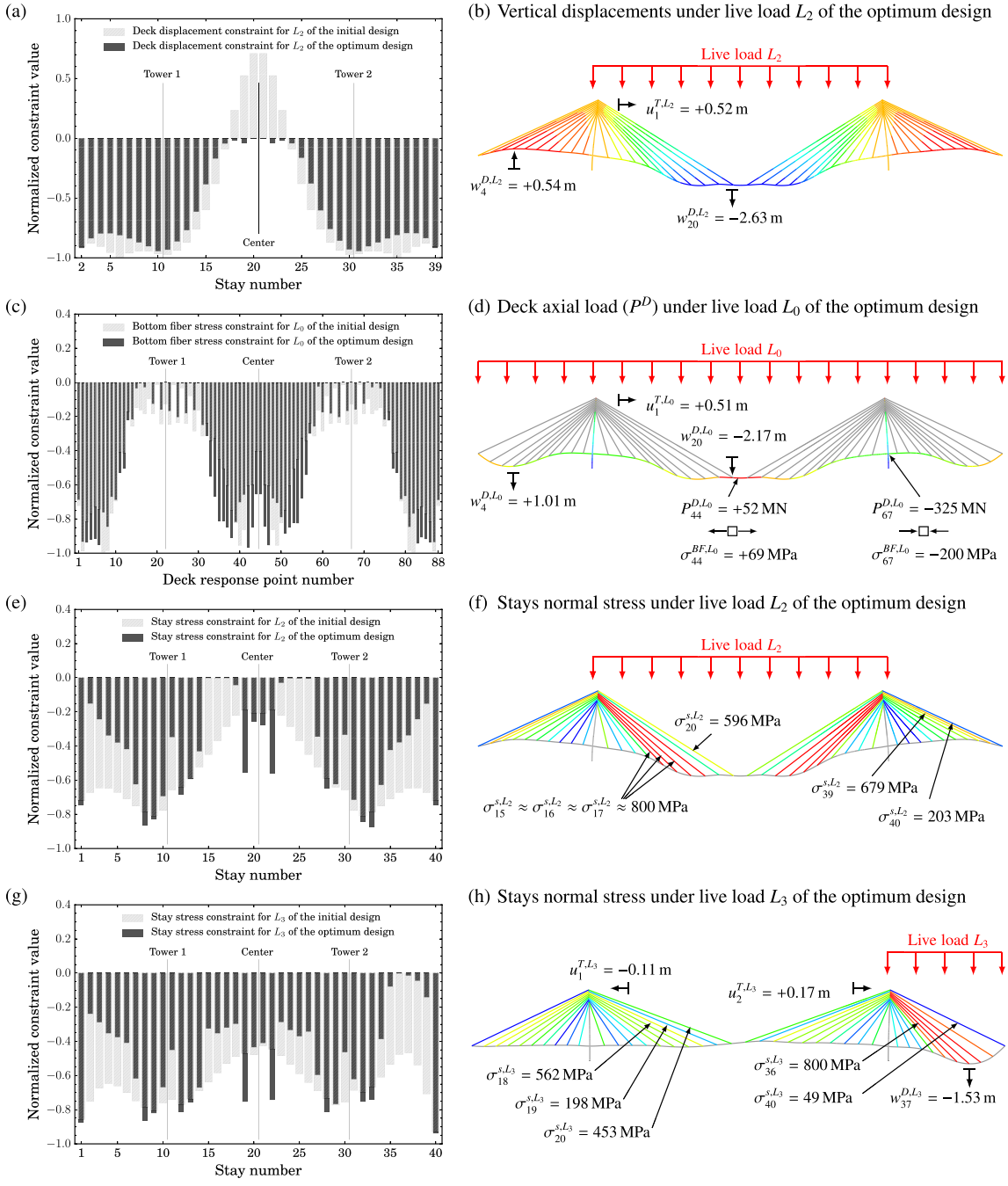

Fig. 11. Subset of the most representative structural responses and design constraints. On the left side (a, c, e, and g), the values of the structural design constraints for the initial and optimum design are compared. On the right side (b, d, f, and h), the structural behavior of the optimum design obtained with the FEM with a deformation scale factor 50 is provided. Figures (a) and (b) show the deck displacements for load case L_2 (Eq. (4)); (c) shows the deck bottom fiber stress constraint for load case L_0 (Eq. (7)); (d) shows the deck axial load for load case L_0, which condition the top and bottom fiber stress of the deck; and (e), (f), (g), and (h) shows the stress in the stays for load cases L_2 and L_3 (Eq. (8)). (For interpretation of the references to color in this figure legend, the reader is referred to the web version of this article.)

Figs. 10 and 11 show the values of a subset of structural performance-related constraints (see Eqs. (2) to (9)), which depend on the gravitational load cases described in Section 6.1. It can be seen in Fig. 10 that the constraints related to the horizontal displacement of the top of the towers (Eqs. (3) and (5)) are only active for the load case L_2, and close to be active for the self-weight load case. Regarding the vertical displacements of the deck (Eq. (4)), it is shown in Fig. 11 (a) that this constraint is active in the main span for the load case L_0. Also, the deck stress constraints (Eqs. (6) and (7)) play an important role in the optimization since they constraint the admissible value of the deck plate thickness. It can be observed in Fig. 11 (c) that the stress constraint at the bottom fiber of the deck for load case L_0 is active in the neighborhoods of the towers. This is the classical behavior of cable-stayed bridges, since the cable-supporting system generates high normal stress levels in the deck position next to the towers, as described in Fig. 11 (d). On the other hand, Fig. 11 (e) and (g) show the values of the stays' stress constraints (Eqs. (8) and (9)) for loads L_2 and L_3, respectively. For these constraints, the three load cases L_1, L_2 and L_3 are active at different locations of the deck, highlighting the need for considering all the relevant gravitational load cases in the optimization problem, as well as a relatively large number of control points along the deck.

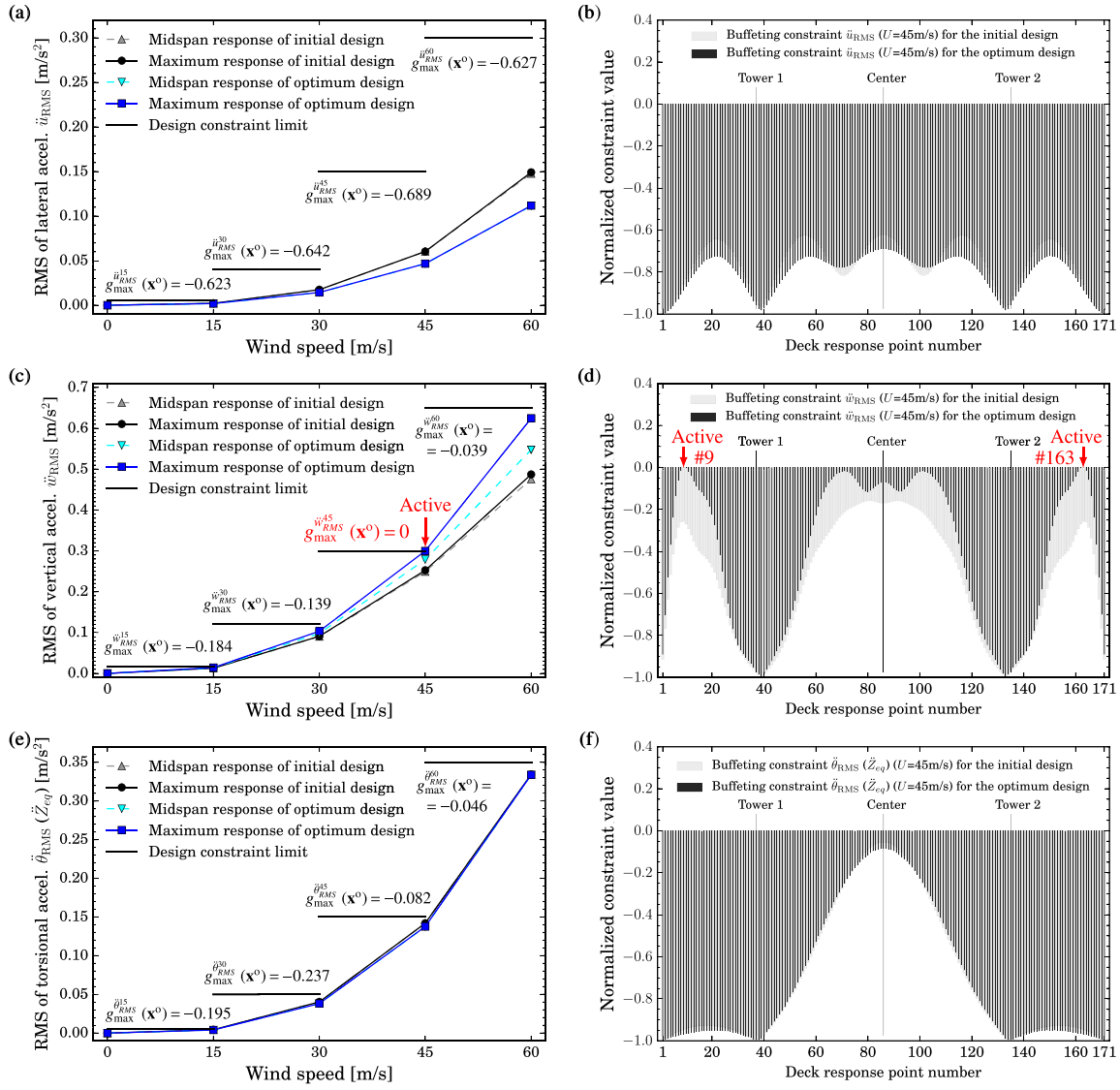

Fig. 12. Buffeting RMS of accelerations constraints (Eqs. (10) to (12)) for the initial and optimum designs. Figures (a), (c), and (e) shows the buffeting responses versus the wind speed. Figures (b), (d), and (f) show the buffeting constraint along the deck for wind velocity $U = 45\,\mathrm{m/s}$.

It can be observed in Figs. 10 and 11 that kinematic and stress constraints at the deck, towers, and stays are active. It is important to remark that all constraints must be considered in the optimization process in order to achieve optimum designs with an adequate performance level for all responses, independently of their nature. In general, the behavior of the bridge under the gravitational loads is similar to the application case reported in Cid Montoya et al. [38].

Fig. 12 reports the design constraints related to the buffeting accelerations formulated in Eqs. (10) to (12) with the limit values indicated in Table 4. Fig. 12 (a), (c), and (e) show the bridge buffeting responses in terms of RMS of accelerations at midspan and the maximum response found along the deck as a function of the wind velocity for both initial and optimum designs. Also, the adopted limit values reported in Table 4 and the highest value of the normalized constraints (Eqs. (10) to (12)) are indicated. The value of these normalized constraints along the deck are shown in Fig. 12 (b), (d), and (f) for wind velocity $U = 45\,\mathrm{m/s}$. It is shown in Fig. 12 (d) that the design is driven by the vertical acceleration constraint for $U = 45\,\mathrm{m/s}$ at the lateral spans, although this constraint is also close to getting active at the main span. The role of the vertical constraint for $U = 45\,\mathrm{m/s}$ at the optimum design and the optimization process is highlighted in Fig. 8 (b), whose convergence is plotted along with the shape design variables, showing the influence of this constraint on both B and H design variables. The fact of having the maximum response at different locations along the deck highlights the need for imposing a large number of design constraints along the deck in the optimization process in order to guarantee that the acceleration at any location along the deck never exceeds the design limit, as formulated in Eqs. (10) to (12). Furthermore, other constraints are close to get active at the optimum design, such as the vertical constraint for $U = 60\,\mathrm{m/s}$, and torsional constraints for $U = 45\,\mathrm{m/s}$ and $60\,\mathrm{m/s}$. The torsional response shows a one-wave response type, which means that the midspan constraint is representative of the buffeting performance for this DoF. On the other hand, it is shown that the lateral constraints are irrelevant for the definition of the optimum design.

In order to better understand how the buffeting design constraints in terms of RMS have been modified throughout the optimization process, it is interesting to analyze the changes in the PSDs of the buffeting accelerations. Fig. 13 compares the PSDs of vertical accelerations for the initial and optimum designs at midspan (control point #86) and control point #163 (symmetric of control point #9), which is the deck cross-section where the vertical buffeting constraint is active at $U = 45\,\mathrm{m/s}$, as shown in Fig. 12 (d). The vertical PSD at midspan (section

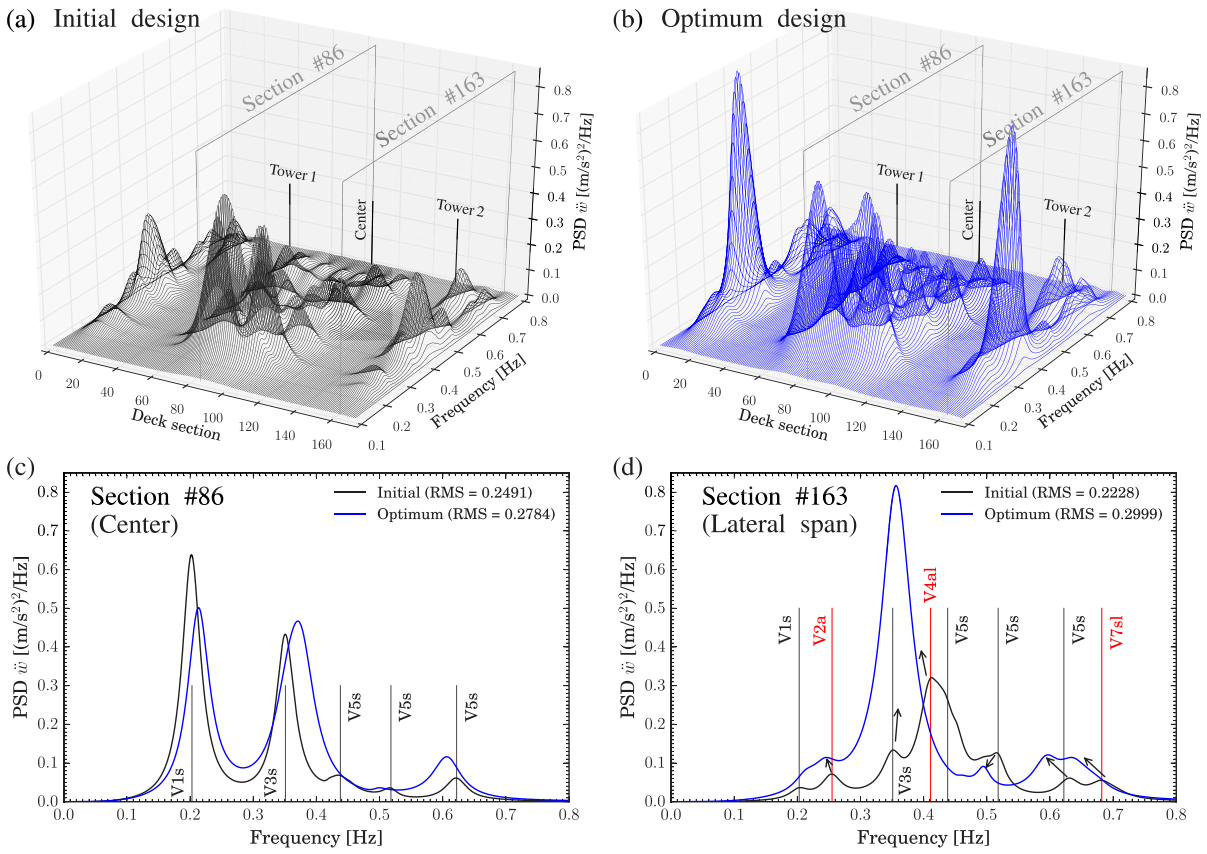

Fig. 13. PSDs of vertical accelerations at wind velocity $U = 45$ m/s for the initial and optimum designs: (a) and (b) show the PSD value for each deck section and frequency; (c) compares the PSD at midspan (section #86); and (d) compares the PSD at section #163 (symmetric of #9). The most influential natural frequencies of the initial design are indicated (see Table 1). Values of RMS of accelerations in m/s^2. (For interpretation of the references to color in this figure legend, the reader is referred to the web version of this article.)

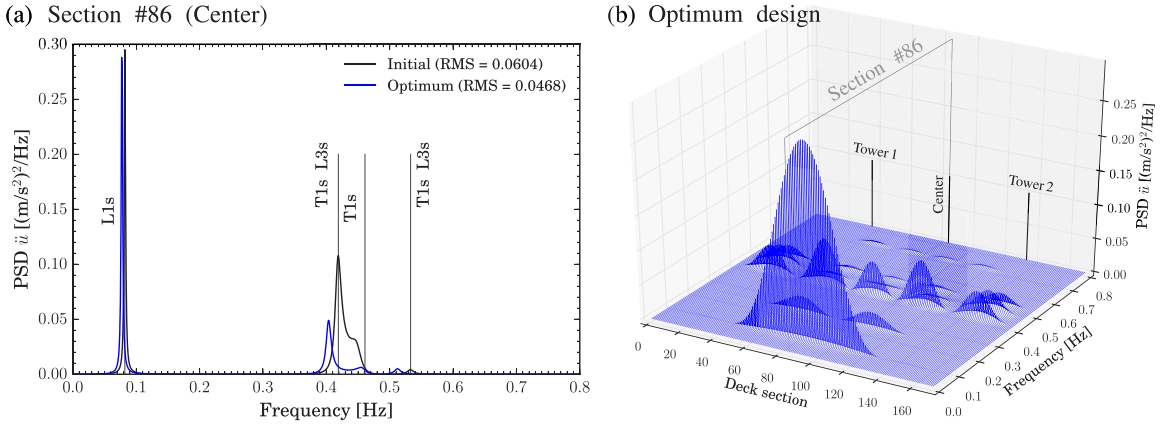

Fig. 14. PSDs of horizontal accelerations at wind velocity $U = 45$ m/s: (a) shows a comparison of the initial and optimum design at midspan (section #86); and (b) shows the value of the PSD for each deck section and frequency value. (For interpretation of the references to color in this figure legend, the reader is referred to the web version of this article.)

#86) is slightly modified along the optimization process, particularly the peaks related to modes "V1s", "V3s", and "V5s", as shown in Fig. 13 (c). This leads to a moderate increase in the value of the vertical RMS, which has no influence on the design optimization. However, at deck control point #163, the maximum allowed value of RMS is reached, as it can be seen in Fig. 13 (d), and therefore the constraint is active, as shown in Fig. 12 (d). It can be observed that the PSD of control point #163 is different from the PSD at midspan, where the main symmetric vertical modes are more influential. Both the symmetric vertical modes (indicated in black color) and modes "V2a", "V4al" and "V7sl" (in red color) are influential on the response. This is so because these last three modes present a one-wave response over the lateral span, as shown in

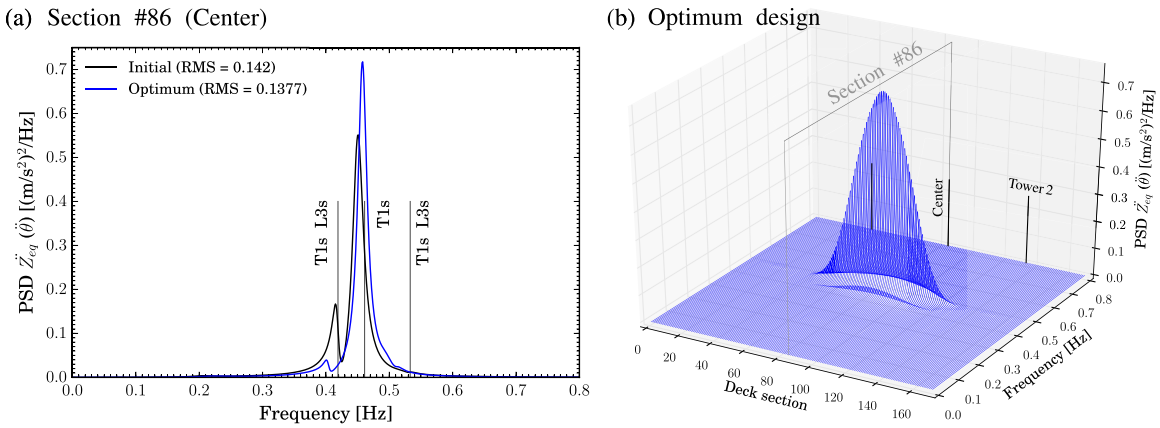

Fig. 15. PSDs of torsional accelerations at wind velocity $U = 45$ m/s: (a) shows a comparison of the initial and optimum design at midspan (section #86); and (b) shows the value of the PSD for each deck section and frequency value. (For interpretation of the references to color in this figure legend, the reader is referred to the web version of this article.)

Fig. 4. In the initial design, modes "V5s" and "V4al" are coupled, giving place to the shape shown in Fig. 12 (d) (see Fig. 4). At the optimum design, modes 8, 9, and 10 are coupled since they are all vertical modes and have very similar frequencies (see Table 1), giving place to the dominant peak at 0.355 Hz shown in Fig. 13 (d), which can be clearly identified in the lateral spans in Fig. 13 (b).

However, while the vertical response of the optimum design is higher than the one obtained for the initial design, the RMS of lateral and torsional of accelerations have been reduced after the optimization process. It must be noted that the goal of the optimization algorithm is to reduce the material of the structure, and it only modifies the bridge design due to the buffeting responses when these design constraints are violated. Therefore, it is not a problem that the vertical response increases, as long as the maximum allowed value for the RMS is not surpassed.

On the other hand, the lateral and torsional buffeting responses decreased after the optimization, as anticipated in Fig. 12. The PSD of lateral acceleration is dominated by the influence of the first symmetric lateral mode at the main span ("L1s") and the pure torsional ("T1s") and lateral–torsional ("T1s L3s" and "T1s L3s") modes. The lateral–torsional modes, which provide the largest contribution to the RMS, have several waves along the deck, as shown in Fig. 14. This fact explains the distributed response along the entire deck reported in Fig. 12 (b). On the contrary, the PSD of torsional acceleration is only relevant at the main span since the largest contribution to the RMS is provided by the pure torsional mode ("T1s"), as shown in Fig. 15.

7. Discussion: Influence of the aeroelastic design constraints on the optimum design

7.1. Sets of maximum allowed values for the buffeting design constraints

Aiming to analyze the influence of the buffeting constraints on the deck shape design, and the ability of the deck shape variables to handle aeroelastic constraints, four additional optimization cases have been studied considering different sets of the maximum allowed values for the buffeting constraints. These sets are described in Table 6. It must be noted that Set #2 is the one previously reported in Section 6.2 (see Table 4), and it is provided here for completeness.

7.2. Optimum aero-structural designs

The optimum designs obtained from the aero-structural optimization, for the sets of buffeting constraints given in Table 6, are reported in Table 7. In this table, the optimum design values obtained for the stays are summarized by means of the backstay average cross-section area $\overline{A^B}^o$, the average area of the other 38 stays $\overline{A^s}^o$, and the average value of the prestressing forces of all the stays of the bridge $\overline{N}^o$. Note that the symbol ^{o}, when referred to any property or design variable of the bridge, denotes the optimum aero-structural design, while the symbol * stands for the optimum structural design, as indicated in Section 5.2. The buffeting constraints that become active at the end of each optimization process are also listed in Table 7. The design constraints related to gravitational loads present similar results as those shown in Figs. 10 and 11.

7.3. Analysis of the optimum deck geometries

The buffeting responses are mainly controlled in this particular problem by the deck shape design variable B, while H takes the maximum allowed value in all the studied cases. This is so because higher values of H result in stiffer and lighter deck cross-sections, without noticeably worsening the aerodynamic responses.

Fig. 16 sketches the optimum geometries compared with the geometry of the initial deck shape design in order to point out the differences introduced by the optimization algorithm for each case. Based on the values adopted for each set of constraints (Table 6), it can be inferred, in general terms, that for more demanding aeroelastic constraints, more streamlined deck cross-sections are required, but always providing high stiffness by increasing the deck depth, since this makes possible to reduce the deck plates thickness and consequently reduce the objective function. This is true while the optimum designs are located over $\mathcal{S}^*$. When more demanding constraints are adopted, the optimization algorithm must find the balance between the deck shape and size to obtain efficient designs that fulfill all structural and aeroelastic design constraints, as was the case of the set #5. This will be discussed in detail below.

7.4. Interpretation from the optimum design space $\mathcal{S}^*$ perspective

The relevance of the deck shape design variables in the aeroelastic design of long-span bridges, and their relationship with the aeroelastic design constraints, was introduced in the above paragraphs. Other size-related design variables, such as the cable-supporting system and deck plates thickness, are controlled by the structural design constraints, and their optimum values (see Table 7) are in accordance with the optimum structural design obtained for those deck shapes, as reported in Section 5. Hence, the optimum designs can be interpreted taking advantage of the optimum design space $\mathcal{S}^*$ concept.

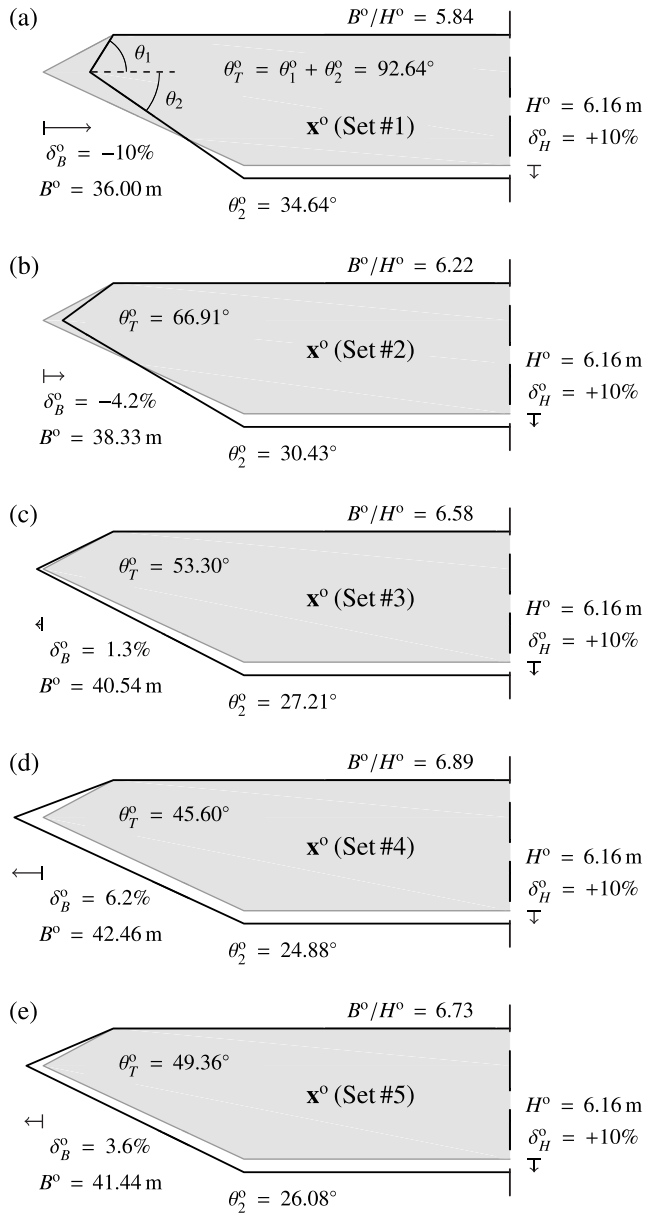

Fig. 16. Geometry of the optimum deck cross-sections obtained for each set of constraints reported in Table 6 (in black) compared with the initial design (in gray, see Fig. 3).

Fig. 17 shows the optimum design space S^* for the five sets of constraints considered. In this figure, the objective function F over S^* (previously reported in Fig. 5) is represented as contour lines in order to help to identify the most adequate designs in terms of F. The projections of each set of buffeting constraints over S^* are plotted in these figures, as explained in Fig. 7, aiming to define the feasible and unfeasible design regions. Furthermore, the initial and optimum designs, and the convergence of B and H, are shown.

In the optimization problem considering Set #1, no buffeting constraint is active, and the optimum design is only conditioned by structural constraints, so the optimum deck shape design is the one that provides the lowest value of the objective function, that is $B = 36\,m$ and $H = 6.16\,m$ (see Fig. 17). This design is very interesting because it shows the kind of deck shape design that structural design constraints demand: the highest stiffness with the lowest amount of material, without any concerns about the degree of bluffness of the deck cross-section geometry.

On the other hand, the designs obtained when the aeroelastic constraints are active are commented on in the following paragraphs. They can be compared with the design obtained from set #1 in order to understand the role of the aeroelastic constraints in the deck shape design.

In the case of set #2, which was previously analyzed in Section 6.2, the optimization algorithm found the optimum design at $B^o = 38.327\,m$ and $H^o = 6.16\,m$, finding a compromise between minimizing the objective function and accomplishing the vertical buffeting constraint for $U = 45\,m/s$, as shown in Fig. 17. The optimum design was found after several iterations of the shape design variables around the neighborhood of the optimum design, as is also shown in Fig. 8 (b), where it can be seen that the width of the section plays a crucial role to achieve the minimum value of F without violating the buffeting constraint. Furthermore, the role of the active buffeting constraint to define the feasible design domain, and how this impacts the value of the objective function at the optimum design, are graphically analyzed in Fig. 18.

A similar situation is found for the set of buffeting constraints #3. However, the maximum acceleration values adopted in this case are more demanding, hence the algorithm needs to modify the deck cross-section to produce a more streamlined geometry (increasing B) that reduces the buffeting response, even though this implies an increase in the value of F (see Table 7). This situation is depicted in Fig. 19, where it can be seen that the active aeroelastic constraint is $g^{\ddot{w}^{60}_{RMS}}(\mathbf{x}^*)$, since in this case the constraint at $U = 60\,m/s$ is more demanding than at $U = 45\,m/s$.

The optimum aero-structural designs found for the first three sets of buffeting constraints studied so far are located over the optimum design space S^*. In other words, these designs are on the optimum design surface that would be found in an structural optimization problem with the same structural constraints for those deck shape geometries, as described in Section 5.2 and in Cid Montoya et al. [38]. Hence, $F(\mathbf{x}^o) \approx F(\mathbf{x}^*)$. However, when more demanding aeroelastic design constraints are adopted, the optimum aero-structural design would need to move away from the structural optimum surface in order to fulfill the aeroelastic constraints, resulting in $F(\mathbf{x}^o) > F(\mathbf{x}^*)$. This is the case of the optimization results obtained for sets #4 and #5.

For set #4, no feasible design region can be identified on S^* (see Fig. 17) due to the more demanding aeroelastic design constraint. Therefore, the algorithm needs to modify all the size-related design variables (mainly the deck plate thickness), along with the deck shape design variables, to fulfill all the structural and aeroelastic requirements. The role of the aeroelastic constraints is graphically represented in Fig. 20. The buffeting design constraints $g^{\ddot{w}^{60}_{RMS}}(\mathbf{x}^*)$ and $g^{\ddot{\theta}^{60}_{RMS}}(\mathbf{x}^*)$ over S^* are represented in Fig. 20 (a). It is noteworthy that $g^{\ddot{w}^{60}_{RMS}}(\mathbf{x}^*)$ is violated in the whole shape space S^* except in the neighborhoods of $\delta_B = +10\%$ & $\delta_H = +10\%$, while $g^{\ddot{\theta}^{60}_{RMS}}(\mathbf{x}^*)$ is violated for designs with high values of δ_B. On Fig. 20 (b), the optimum aero-structural design is plotted along with the value of $F(\mathbf{x}^*)$ for the optimum structural designs on S^*. It can be seen that the objective function associated with the aero-structural optimal design $F(\mathbf{x}^o)$ is larger than the value of F associated with the optimum structural design $F(\mathbf{x}^*)$ for the same values of the shape design variables B and H due to the larger thickness required. This is the result of the modifications made on the design to fulfill the aeroelastic design constraints that cannot be managed only by modifications on the deck shape variables. Hence, the optimum aero-structural design is in this case above S^*, since $F(\mathbf{x}^o) > F(\mathbf{x}^*)$.

The situation reported for set #4 is even clearer at the optimum aero-structural design obtained for the set #5. Three buffeting constraints are simultaneously active here ($g^{\ddot{w}^{60}_{RMS}}(\mathbf{x}^*)$, $g^{\ddot{\theta}^{45}_{RMS}}(\mathbf{x}^*)$ and $g^{\ddot{\theta}^{60}_{RMS}}(\mathbf{x}^*)$), and the value of the thickness is increased (see Table 7) compared to the structural optimum thickness expected for that deck shape design, that would be around $t^* \approx 2.175\,cm$ (see Fig. 5) while the aero-structural optimum is $t^o = 2.3\,cm$. In this case, the increase in F and t are higher than for set #4, since the requirements posed by the aeroelastic constraints are higher.

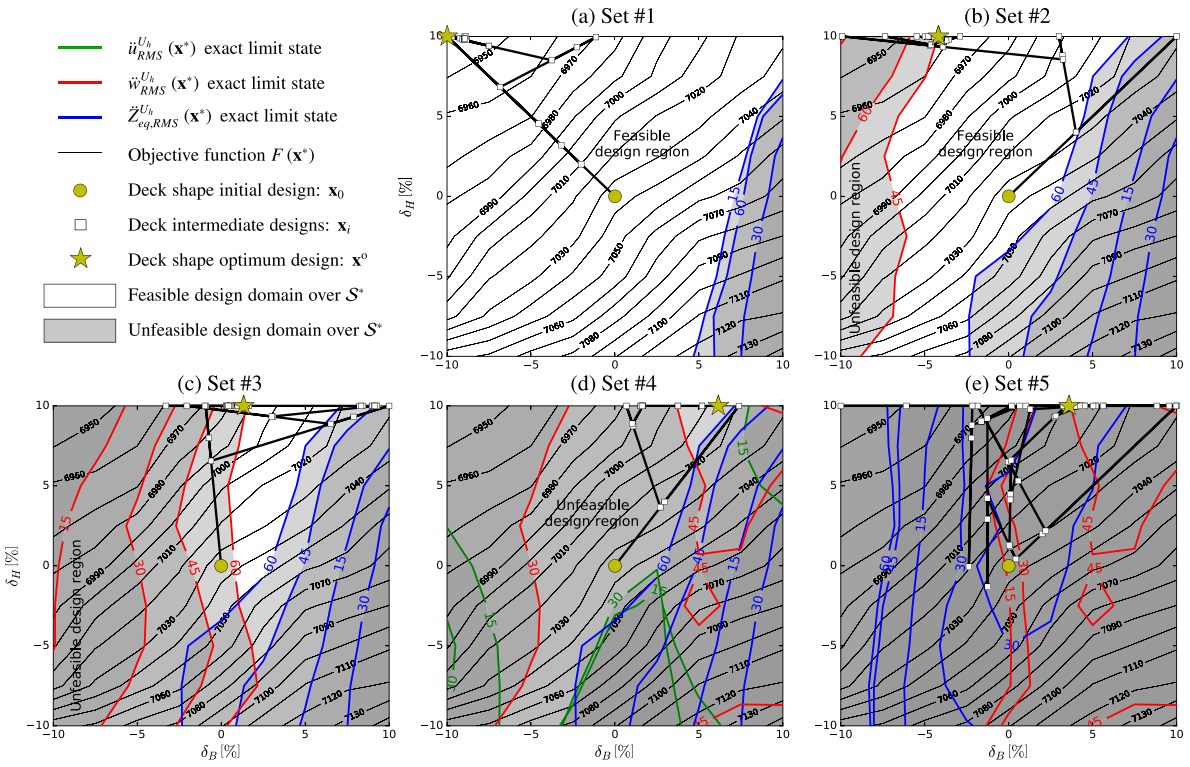

Fig. 17. Optimum deck shape design obtained for some of the buffeting constraints set. Buffeting constraints are represented over the shape design space S^* following the procedure adopted in Fig. 7: lateral in green, vertical in red and torsional in blue. The initial deck shape design is indicated by a yellow square and the optimum deck shape design by a yellow star, while the evolution along the optimization process is represented by white squares. (For interpretation of the references to color in this figure legend, the reader is referred to the web version of this article.)

Table 6
Sets of values for the buffeting constraints (Eqs. (10) to (12)).

Constraint set #	RMS of lateral accel. [m²/s]				RMS of vertical accel. [m²/s]				RMS of torsional accel. Z_{eq} [m²/s]			
	$\ddot{u}_{15}$	$\ddot{u}_{30}$	$\ddot{u}_{45}$	$\ddot{u}_{60}$	$\ddot{w}_{15}$	$\ddot{w}_{30}$	$\ddot{w}_{45}$	$\ddot{w}_{60}$	$\ddot{\theta}_{15}$	$\ddot{\theta}_{30}$	$\ddot{\theta}_{45}$	$\ddot{\theta}_{60}$
1	0.0050	0.04	0.15	0.3	0.0200	0.15	0.350	0.75	0.0050	0.05	0.200	0.40
2[a]	0.0050	0.04	0.15	0.3	0.0175	0.12	**0.300**	0.65	0.0050	0.05	0.150	0.35
3	0.0050	0.04	0.15	0.3	0.0150	0.10	0.275	**0.55**	0.0050	0.05	0.150	0.35
4	0.0025	0.02	0.15	0.3	0.0200	0.10	0.250	**0.50**	0.0050	0.05	0.150	0.35
5	0.0050	0.04	0.15	0.3	0.0125	0.09	0.250	**0.50**	0.0040	0.04	**0.125**	**0.30**

The constraints active in the optimization process are indicated in bolt and underlined (see Table 7).
[a]Set #2 is the case analyzed in Section 6 and it is included here as a reference.

Table 7
Subset of optimum values of the main design variables for the aero-structural optimization considering the set of constraints reported in Table 6.

Constraint Set #	Iter.	F^o [m³]	B^o [m]	H^o [m]	t^o [cm]	$\overline{A^B}^o$ [m²]	$\overline{A^s}^o$ [m²]	$\overline{N}^o$ [MPa]	Active buffeting constraints[b]
1	57	6937.02	36.000	6.160	2.407	0.5412	0.0394	490.3	None
2[a]	81	6964.18	38.327	6.160	2.303	0.5451	0.0403	475.5	$\ddot{w}^l_{45}$
3	68	6998.57	40.536	6.160	2.209	0.5410	0.0409	456.0	$\ddot{w}^l_{60}$
4	55	7038.14	42.462	6.160	2.153	0.5395	0.0397	453.6	$\ddot{w}^l_{60}$
5	79	7306.71	41.438	6.160	2.290	0.5160	0.0423	443.4	$\ddot{w}^l_{60}$, $\ddot{\theta}^m_{45}$ & $\ddot{\theta}^m_{60}$

[a]Set #2 is the case analyzed in Section 6 and it is included here as a reference.
[b]w = vertical response, θ = rotational response, l = active constraint at lateral span, m = active constraint at main span. The number indicates the wind velocity of the active constraint.

7.5. Identification of three different types of aero-structural shape optimization problems

The behavior of the optimization algorithm for different sets of design constraints limit values has been discussed in the previous sections. Based on the information provided by the structural optimum shape space S^* and the similitude or differences between the aero-structural and purely optimum structural designs, three different types of aero-structural shape optimization problems can be identified, which are conceptually described below:

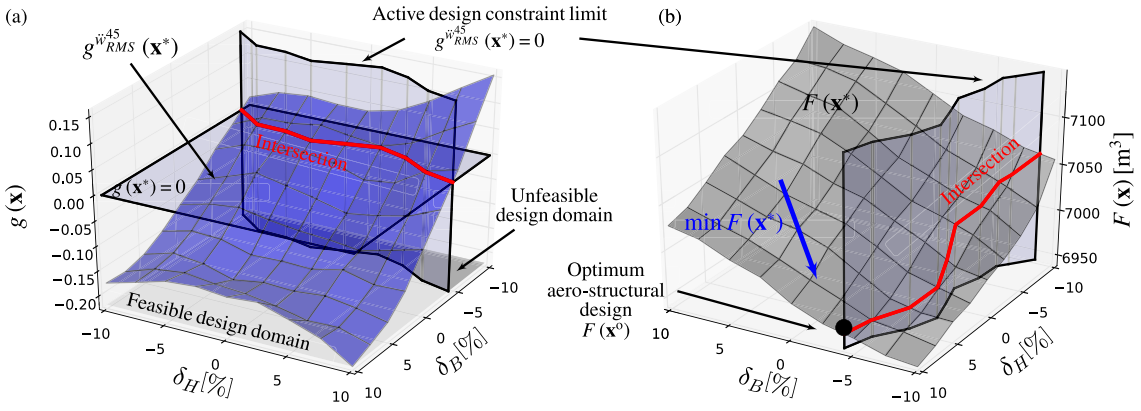

Fig. 18. Interpretation of the optimum design obtained for Set #2. The maximum RMS of the vertical acceleration at $U = 45\,\mathrm{m/s}$ (Eq. (11)) is depicted to show how it conditions the optimum value of the objective function $F(\mathbf{x})$ (Eq. (1), Fig. 5). It must be noted that Figure (a) is rotated 90° to facilitate its interpretation.

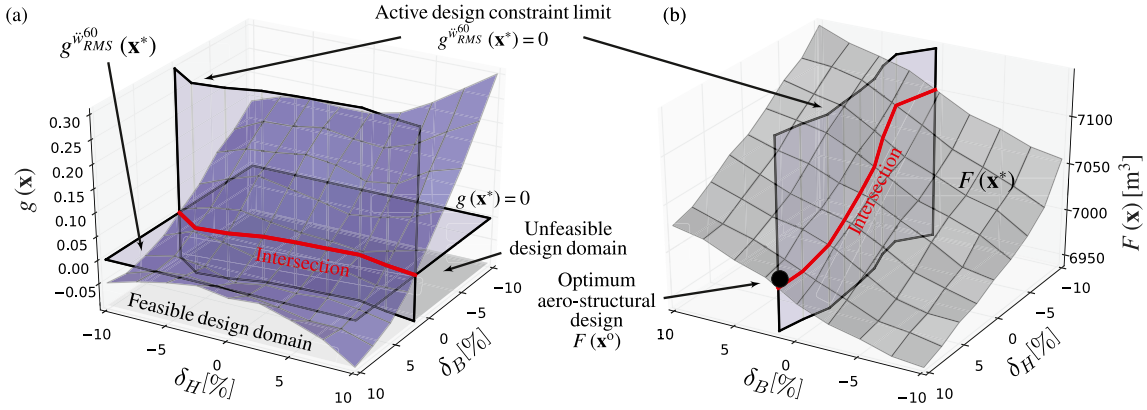

Fig. 19. Interpretation of the optimum design obtained for Set #3. The maximum RMS of vertical acceleration at $U = 60\,\mathrm{m/s}$ (Eq. (11)) is depicted in Figure (a) to show how it conditions the optimum value of the objective function $F(\mathbf{x})$ (Eq. (1), Fig. 5) in Figure (b).

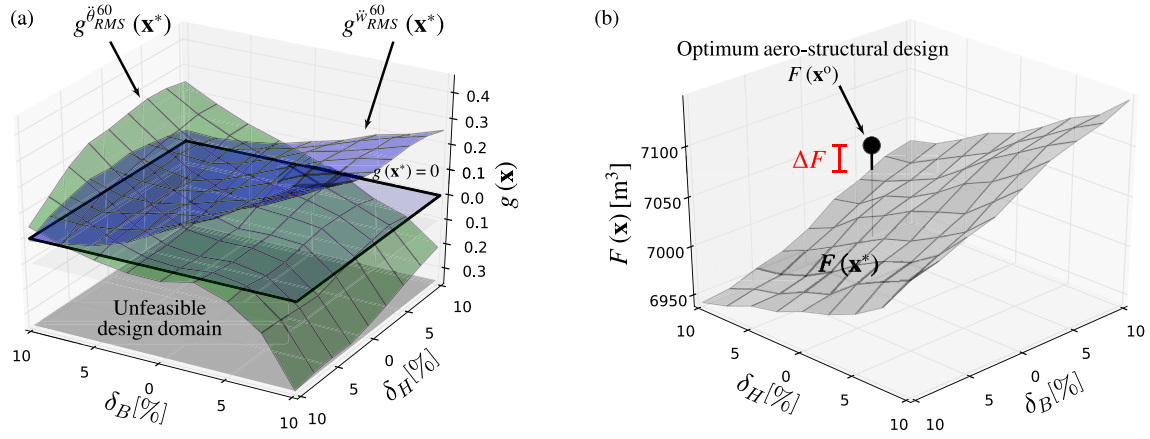

Fig. 20. Interpretation of the optimum design obtained for Set #4: (a) shows the most relevant aeroelastic design constraints ($g^{\ddot{w}^{60}_{RMS}}(\mathbf{x}^*)$ and $g^{\ddot{\theta}^{60}_{RMS}}(\mathbf{x}^*)$) over S^*, while (b) shows the value of $F(\mathbf{x}^o)$ obtained in the aero-structural optimization compared with the value of $F(\mathbf{x}^*)$ of the optimum structural designs. The difference is expressed as $\Delta F = F(\mathbf{x}^o) - F(\mathbf{x}^*)$.

- Type I: Aeroelastic constraints are not active at the optimum. Only the structural constraints are active. In this case, the aero-structural optimum deck shape corresponds to the deck geometry with the lowest value of the objective function in S^* (see Fig. 17). Hence, the optimum aero-structural design will be the same as the optimum structural design considering the same deck shape, therefore $F(\mathbf{x}^o) \approx F(\mathbf{x}^*)$. This was the case of the optimization problem considering the set #1 of design constraints (see Table 6).
- Type II: Aeroelastic and structural constraints are both active and the optimum aero-structural design is on S^*. In this situation, one or more aeroelastic constraints are active at the optimum design, and they are controlled mainly by the deck shape design

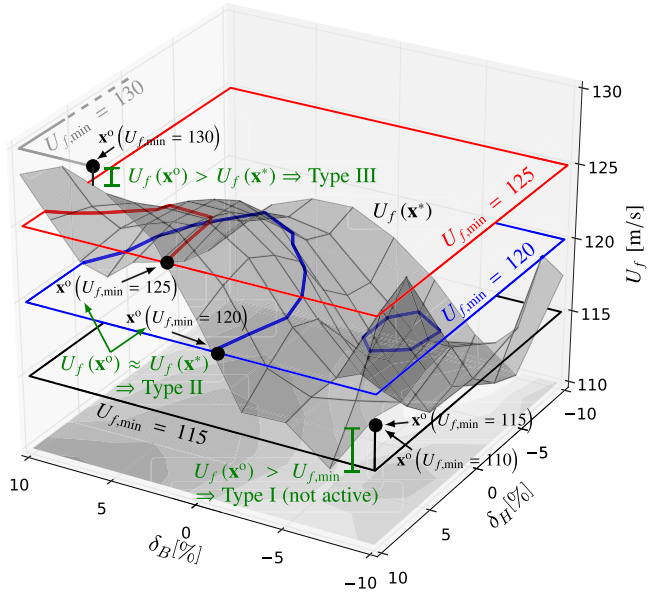

Fig. 21. Identification of different types of aero-structural optimization problems among the five cases studied in Cid Montoya et al. [38]. (For interpretation of the references to color in this figure legend, the reader is referred to the web version of this article.)

variables. The optimum design is similar to the one that would be obtained conducting an structural optimization considering the deck cross-section as a fixed parameter, since the optimum aero-structural design is on S^*. Hence, $F(\mathbf{x}^o) \approx F(\mathbf{x}^*)$. The optimum deck cross-section will be the one with the lowest value of F in the feasible design regions over S^*, or, in other words, where the aeroelastic constraints are not violated $g^{ae} \leq 0$ (see Fig. 17). This was the case of the optimization problem solved for sets #2 (see Fig. 18) and #3 (see Fig. 19).

- Type III: Aeroelastic and structural constraints are both active and the optimum aero-structural design is above S^*. Hence, the optimization algorithm needs to use all the available design variables in the problem to accomplish the aeroelastic requirements. The optimum deck shape is the one that makes it possible to reach a design with the lowest objective function value that fulfills the aeroelastic constraints, and the most effective deck shape design to achieve this goal is the one where the value of g^{ae} is the lowest so the size design variables are as low as possible. Consequently, the bridge optimum design will be different from the structural optimization considering the deck cross-section as a fixed parameter, since the size variables are adjusted to fulfill all aeroelastic design constraints. This can be appreciated in Fig. 20, where the optimum aero-structural design F^o is above the value of F^* for the designs in S^*. Therefore, $F(\mathbf{x}^o) > F(\mathbf{x}^*)$. Examples of Type III are sets #4, where only one aeroelastic design constraint is active at the optimum (see Fig. 20), and #5, where three aeroelastic constraints are simultaneously active for the optimum design.

The same pattern can be identified in the results reported in Cid Montoya et al. [38], where the aero-structural optimization was performed considering flutter as aeroelastic design constraint and five different values of minimum flutter velocity were imposed: $U_{f,\min} = [110, 115, 120, 125, 130]$ m/s. This is represented in Fig. 21, where the aero-structural optimum designs (black dots) are compared with the flutter velocity response surface over S^* (gray surface), and the constraint limit for each case in terms of minimum flutter velocity (horizontal flat planes in gray, red, blue and black). The first two examples ($U_{f,\min} = 110$ m/s and 115 m/s) can be classified as Type I, since $U_f(\mathbf{x}^o) \approx U_f(\mathbf{x}^*) \approx 118.8$ m/s $> U_{f,\min}$. The situation for the application examples considering $U_{f,\min} = 120$ m/s and 125 m/s corresponds to Type II, since the flutter constraint is active at the optimum, and $U_f(\mathbf{x}^o) \approx U_f(\mathbf{x}^*) \approx U_{f,\min}$. The last example, $U_{f,\min} = 130$ m/s, can be classified as Type III, hence, $U_f(\mathbf{x}^o) \approx U_{f,\min} > U_f(\mathbf{x}^*)$, since the algorithm required to increase to deck plate thickness to increase the flutter velocity and reach the minimum imposed value.

8. Concluding remarks

This paper discussed the tailoring of deck shape design variables to mitigate aeroelastic responses of bridges using aero-structural optimization. With this aim, an efficient numerical design framework was introduced to carry out the aero-structural optimization of bridges with streamlined decks considering structural and buffeting constraints. The methodology includes deck shape design variables as well as the size related design variables. It permits the application of parallelization techniques at both the optimization and response evaluation levels, which makes it possible to obtain optimum aero-structural designs of full bridges with modest computational effort.

A long-span cable-stayed bridge has been successfully optimized, reducing the total material volume by 8.6%, while meeting all imposed structural and aeroelastic design constraints. This has been achieved by increasing the depth, slightly reducing the width and the deck plate thickness, and redistributing the stays' cross-section area along the deck. In this case study, it has been found that the deck shape design is determined mainly by its width, since the fairing angle of the deck cross-section is very sensitive to the value of this deck shape variable, and consequently B controls the aerodynamic responses. Particularly, both the vertical and torsional buffeting RMS of accelerations are very sensitive to the value of B, and therefore the optimization algorithm uses this shape variable to accomplish the aeroelastic requirements.

Moreover, the relationship between the aeroelastic design constraints and the aero-structural optimum deck shape designs has been analyzed by optimizing the bridge adopting different sets of thresholds in the aeroelastic design constraints. Different results have been obtained for each case studied and it has been found that the role of the deck shape design variables may change depending on the level of demand posed by the aeroelastic design constraints. Three different types of aero-structural optimization problems have been identified, where the optimization algorithm manages the design variables and design constraints in different ways. Hence, a classification of three different aero-structural optimization problems has been proposed. The implication of the concept derived from this classification can be generalized for other wind-resistant design problems involving shape design variables.

Future research will address the development of a comprehensive aero-structural optimization framework including all aeroelastic responses that may impact the bridge stability and performance, including flutter, nonlinear aerostatic stability, buffeting, and VIV. Furthermore, additional advanced numerical frameworks must be developed building upon the one proposed in this study to deal with the nonlinear aeroelastic effects that can be observed in bluff body aerodynamics.

CRediT authorship contribution statement

M. Cid Montoya: Conceptualization, Methodology, Software, Formal analysis, Writing – original draft, Writing – review & editing, Visualization. **S. Hernández:** Conceptualization, Supervision, Writing – review & editing. **A. Kareem:** Conceptualization, Supervision, Writing – review & editing.

Declaration of competing interest

The authors declare that they have no known competing financial interests or personal relationships that could have appeared to influence the work reported in this paper.

Acknowledgments

M. Cid Montoya was funded by the Xunta de Galicia (Galician regional government) and the Fulbright Scholar Program with reference ED481B2018/053. S. Hernández was funded by the Xunta de Galicia, including FEDER funding, with reference ED431C 2017/72. A. Kareem especially thanks NSF support under grant CMMI #1612843. The authors fully acknowledge the support received.

References

[1] Schmit LA. Structural Design by Systematic Synthesis. In: Proceedings of the 2nd Conference on Electronic Computation, ASCE, 1960.
[2] Schmit LA. Structural synthesis. its genesis and development. AIAA J 1981;19(10):1249–63.
[3] Hicks RM, Murman EM, Vanderplaats GN. An Assessment of Airfoil Design by Numerical Optimization. Technical report, NASA TM-X-3092, 1974.
[4] Hicks RM, Henne PA. Wing design by numerical optimization. J Aircr 1978;15(7):407–12.
[5] Reuther JJ, Jameson A, Alonso JJ, Rimlinger MJ, Saunders D. Constrained multipoint aerodynamic shape optimization using an adjoint formulation and parallel computers, Part 1. J Aircr 1999;36(1):51–60.
[6] Lyu Z, Kenway GKW, Martins JRRA. Aerodynamic shape optimization investigations of the common research model wing benchmark. AIAA J. 2015;53(4):968–85.
[7] Martins JRRA, Alonso JJ, Reuther JJ. High-fidelity aerostructural design optimization of a supersonic business jet. J Aircr 2004;41(3):523–30.
[8] Jasa JP, Hwang JT, Martins JRRA. Open-source coupled aerostructural optimization using python. Struct Multidiscip Optim 2018;57:1815–27.
[9] Lagaros ND. The environmental and economic impact of structural optimization. Struct Multidiscip Optim 2018;58:1751–68.
[10] Kareem A. Emerging frontiers in wind engineering: Computing, stochastics, machine learning and beyond. J Wing Eng Ind Aerod 2020;206:104320.
[11] Bernardini E, Spence SMJ, Wei D, Kareem A. Aerodynamic shape optimization of civil structures: A CFD-enabled Kriging-based approach. J Wing Eng Ind Aerod 2015;144:154–64.
[12] Elshaer A, Bitsuamlak G, El Damatty A. Enhancing wind performance of tall buildings using corner aerodynamic optimization. Eng Struct 2017;136:133–48.
[13] Ding F, Kareem A. Tall buildings with dynamic facade under winds. Engineering 2020;6(12):1443–53.
[14] Li R, Xu P, Peng Y, Ji P. Multi-objective optimization of a high-speed train head based on the FFD method. J Wing Eng Ind Aerod 2016;152:41–9.
[15] Muñoz Paniagua J, García J. Aerodynamic surrogate-based optimization of the nose shape of a high-speed train for cross-wind and passing-by scenarios. J Wing Eng Ind Aerod 2019;184:139–52.
[16] Horvat M, Bruno L, Khris S, Raffaele L. Aerodynamic shape optimization of barriers for windblown sand mitigation using CFD analysis. J Wing Eng Ind Aerod 2020;197:104058.
[17] Azevedo AFM, Adão da Fonseca A, Oliveira R. Shape optimization of a metallic bridge (original in Portuguese: Optimizaçao da forma de uma ponte metálica). In: Métodos Numéricos En Ingeniería, SEMI. 2002.
[18] Simões LMC, Negrão JHO. Sizing and geometry optimization of cable-stayed bridges. Compt Struct 1994;52(2):309–21.
[19] Baldomir A, Hernández S, Nieto F, Jurado JA. Cable optimization of a long span cable stayed bridge in La Coruña (Spain). Adv Eng Softw 2010;41:931–8.
[20] Hassan MM, Nassef AO, El Damatty AA. Determination of optimum post-tensioning cable forces of cable-stayed bridges. Eng Struct 2012;44:248–59.
[21] Lonetti P, Pascuzzo A. Optimum design analysis of hybrid cable-stayed suspension bridges. Adv Eng Softw 2014;73:53–66.
[22] Fabbrocino F, Modano M, Farina I, Carpentieri G, Fraternali F. Optimal prestress design of composite cable-stayed bridges. Compos Struct 2017;169:167–71.
[23] Arellano H, Tolentino D, Gómez R. Optimum criss crossing cables in multi-span cable-stayed bridges using genetic algorithms. KSCE J Civ Eng 2019;23(2):719–28.
[24] Simões LMC, Negrão JHO. Optimization of cable-stayed bridges subjected to earthquakes with non-linear behaviour. Eng Optim 1999;31(4):457–78.
[25] Ferreira F, Simões L. Synthesis of three dimensional controlled cable-stayed bridges subject to seismic loading. Compt Struct 2020;226:106–37.
[26] Ferreira F, Simões L. Optimum design of a cable-stayed steel footbridge with three dimensional modelling and control devices. Eng Struct 2019;180:510–23.
[27] Martins AMB, Simes LMC, Negrão JHJO. Optimization of cable-stayed bridges: A literature survey. Adv Eng Softw 2020;149:102829.
[28] Larsen A, Larose GL. Dynamic wind effects on suspension and cable-stayed bridges. J Sound Vib 2015;334:2–28.
[29] Jurado JA, Hernández S. Sensitivity analysis of bridge flutter with respect to mechanical parameters of the deck. Struct Multidiscip Optim 2004;27:272–83.
[30] Agar TJA. Aerodynamic flutter analysis of suspension bridges by a modal technique. Eng Struct 1989;11:75–82.
[31] Katsuchi H, Jones NP, Scanlan RH. Multimode coupled flutter and buffeting analysis of the Akashi-Kaikyo Bridge. J Struct Eng 1999;125(1):60–9.
[32] Zhang X-J. Study of design parameters of flutter stability of cable-stayed-suspension hybrid bridges. Wind Struct Int J 2006;9(4):331–44.
[33] Argentini T, Pagani A, Rocchi D, Zasso A. Monte Carlo analysis of total damping and flutter speed of a long span bridge: Effects of structural and aerodynamic uncertainties. J Wing Eng Ind Aerod 2014;128:90–104.
[34] Nieto F, Hernández S, Jurado JA. Optimum design of long-span suspension bridges considering aeroelastic and kinematic constraints. Struct Multidisc Opt 2009;39:133–51.
[35] Kusano I, Baldomir A, Jurado JA, Hernández S. The importance of correlation among flutter derivatives for the reliability based optimum design of suspension bridges. Eng Struct 2018;173:416–28.
[36] Sarkar PP, Caracoglia L, Haan FL, Sato H, Murakoshi J. Comparative and sensitivity study of flutter derivatives of selected bridge deck sections, Part I: Analysis of inter-laboratory experimental data. Eng Struct 2009;31:158–69.
[37] Cid Montoya M, Nieto F, Hernández S, Kusano I, Álvarez AJ, Jurado JA. CFD-based aeroelastic characterization of streamlined bridge deck cross-sections subject to shape modifications using surrogate models. J Wing Eng Ind Aerod 2018;177:405–28.
[38] Cid Montoya M, Hernández S, Nieto F. Shape optimization of streamlined decks of cable-stayed bridges considering aeroelastic and structural constraints. J Wing Eng Ind Aerod 2018;177:429–55.
[39] Chen W-F, Duan L. Bridge Engineering Handbook. CRC Press; 1999.
[40] Scanlan RH. Interpreting aeroelastic models of cable-stayed bridge. J Eng Mech Division, ASCE 1987;113(4):555–75.
[41] Chen X, Kareem A. Advances in modeling of aerodynamic forces on bridge decks. J Eng Mech 2002;128(11):1193–205.
[42] Hui CH, Ding QS, Xu YL. Buffeting response analysis of stonecutters bridge. HKIE Trans 2005;12(2):8–21.
[43] Zasso A, Stoyanoff S, Diana G, Vullo E, Khazem D, Serzan K, Pagani A, Argentini T, Rosa L, Dallaire PO. Validation analyses of integrated procedures for evaluation of stability, buffeting response and wind loads on the Messina Bridge. J Wing Eng Ind Aerod 2013;122:50–9.
[44] Lystad TM, Fenerci A, Øiseth O. Buffeting response of long-span bridges considering uncertain turbulence parameters using the environmental contour method. Eng Struct 2020;213:110575.
[45] ISO 2631, ISO 2631. Mechanical vibration and shock - Evaluation of human exposure to whole-body vibration. Technical report ISO, 2018.
[46] Zhu Q, Xu YL, Shum KM. Stress-level buffeting analysis of a long-span cable-stayed bridge with a twin-box deck under distributed wind loads. Eng Struct 2016;127:416–33.
[47] Repetto MP, Torrielli A. Long term simulation of wind-induced fatigue loadings. Eng Struct 2017;132:551–61.
[48] Stretto di Messina, Stretto di Messina. Messina Strait Bridge: Basis of design and expected performance (original in Italian: Ponte sullo Stretto di Messina: Fondamenti Progettuali e Prestazioni Attese per l'Opera di attraversamento). Technical report, Stretto di Messina Report GCG.F.04.01, 2004.
[49] Larsen A, Poulin S. Vortex-shedding excitation of box-girder bridges and mitigation. Struct Eng Int 2005;15:258–63.
[50] Diana G, Resta F, Belloli B, Rocchi D. On the vortex shedding forcing on suspension bridge deck. J Wing Eng Ind Aerod 2006;94:341–63.
[51] Boonyapinyo V, Lauhatanon Y, Lukkunaprasit P. Nonlinear aerostatic stability analysis of suspension bridges. Eng Struct 2006;28:793–803.
[52] Nagai M, Fujino Y, Yamaguchi H, Iwasaki E. Feasibility of a 1400 m span steel cable-stayed bridge. J Bridge Eng ASCE 2004;9(5):444–52.
[53] Muyl F, Dumas L, Herbert V. Hybrid method for aerodynamic shape optimization in automotive industry. Comput & Fluids 2004;33:849–58.
[54] Mooneghi MA, Kargarmoakhar R. Aerodynamic mitigation and shape optimization of buildings: Review. J Build Eng 2016;6:225–35.
[55] Chehouri A, Younes R, Ilinca A, Perron J. Review of performance optimization techniques applied to wind turbines. Appl Energy 2015;142:361–88.
[56] Skinner SN, Zare-Behtash H. State-of-the-art in aerodynamic shape optimisation methods. Appl Soft Comput 2018;62:933–62.
[57] Cid Montoya M, Hernández S, Nieto F, Kareem A. Aero-structural design of bridges focusing on the buffeting response: Formulation, parametric studies and deck shape tailoring. J Wing Eng Ind Aerod 2020;204:104243.
[58] Kavrakov I, Morgenthal G. A comparative assessment of aerodynamic models for buffeting and flutter of long-span bridges. Engineering 2017;3(6):823–38.
[59] Martins JRRA, Lambe AB. Multidisciplinary design optimization: A survey of architectures. AIAA J 2013;51(9):2049–75.
[60] Scanlan RH. The action of flexible bridges under wind, II: Buffeting theory. J Sound Vib 1978;60(2):201–11.
[61] Diana G, Stoyanoff S, Aas-Jakobsen K, Allsop A, Andersen M, Argentini T, Cid Montoya M, Hernández S, Jurado JA, Katsuchi H, Kavrakov I, Kim H-K, Larose G, Larsen A, Øiseth O, Omarini S, Rocchi D, Svendsen M, Wu T. IABSE task group 3.1 benchmark results. Part 2: Numerical analysis of a 3-degree-of-freedom bridge deck section based on experimental aerodynamics. Struct Eng Int 2020;30(3):411–20.
[62] Vanderplaats GN, Salajegheh E. New approximation method for stress constraints in structural synthesis. AIAA J 1989;27(1):352–8.
[63] Scanlan RH, Tomko JJ. Airfoil and bridge deck flutter derivatives. J Eng Mech Division 1971;97(6):1717–37.